



## Relative effects of open biomass and crop straw burning on haze formation over central and eastern China: modelling study driven by constrained emissions

5 Khalid Mehmood<sup>1\*</sup>, Yujie Wu<sup>1\*</sup>, Liqiang Wang<sup>1</sup>, Shaocai Yu<sup>1,2+</sup>, Pengfei Li<sup>1,3+</sup>, Xue Chen<sup>1</sup>, Zhen Li<sup>1</sup>,  
Yibo Zhang<sup>1</sup>, Mengying Li<sup>1</sup>, Weiping Liu<sup>1</sup>, Yannian Zhu<sup>4</sup>, Daniel Rosenfeld<sup>5</sup>, and John H. Seinfeld<sup>2</sup>

<sup>1</sup>Research Center for Air Pollution and Health; Key Laboratory of Environmental Remediation and Ecological Health, Ministry of Education, College of Environment and Resource Sciences, Zhejiang University, Hangzhou, Zhejiang 310058, P.R. China

10 <sup>2</sup>Division of Chemistry and Chemical Engineering, California Institute of Technology, Pasadena, CA 91125, USA.

<sup>3</sup>College of Science and Technology, Hebei Agricultural University, Baoding, Hebei 071000, P.R. China

<sup>4</sup>Meteorological Institute of Shaanxi Province, 36 Beiguanzhengjie, Xi'an 710015, China

<sup>5</sup>Institute of Earth Sciences, The Hebrew University of Jerusalem, Jerusalem, Israel

15 \*These authors contributed equally to this work.

*Correspondence to:* Shaocai Yu (shaocaiyu@zju.edu.cn); Pengfei Li (lpf\_zju@163.com)

20

25

30



35 **Abstract.** Open biomass burning (OBB) has large potential in triggering local and regional severe haze with elevated fine  
particulate matter ( $PM_{2.5}$ ) concentrations and could thus deteriorate ambient air quality and threaten human health. Open  
crop straw burning (OCSB), as a critical part of OBB, emits abundant gaseous and particulate pollutants, especially in fields  
with intensive agriculture, such as central and eastern China (CEC). However, there are high uncertainties in current OCSB  
and other types of OBB emissions that could drive chemical transport models (CTMs) to fail to evaluate their respective  
40 impacts on haze formations accurately. Satellite retrievals provide an attractive alternative that can be used to simultaneously  
quantify emissions of OCSB and other types of OBB, such as the Fire INventory from NCAR version 1.5 (FINNv1.5),  
which yet generally underestimate their magnitudes due to unresolved small fires. In this study, we selected June in 2014 as  
our study period, which exhibited a complete evolution process of OBB (from June 1 to 19) over CEC. During this period,  
OBB was dominated by OCSB in terms of the number of fire hotspot and associated emissions (74 ~ 94 %), most of which  
45 were located at Henan and Anhui (> 60 %) with intensive enhancements from June 5 to 14 (> 80 %). It is found that OCSB  
presented a generally strong spatiotemporal correlation with regional haze over the central part of CEC (Henan, Anhui,  
Hubei, and Hunan), while other types of OBB emissions had certain influences on Jiangxi, Zhejiang, and Fujian. Based on  
these analyses, we established a constraining method that integrates ground  $PM_{2.5}$  measurements with a state-of-art fully  
coupled regional meteorological and chemical transport model (the two-way coupled WRF-CMAQ) in order to derive  
50 optimal OBB emissions based on FINNv1.5. It is demonstrated that these emissions could allow the model to reproduce  
meteorological and chemical fields over CEC during the study period, whereas original FINNv1.5 underestimated OBB  
emissions by 2 ~ 7 times, depending on specific spatiotemporal scales. The results show that OBB had substantial impacts on  
surface  $PM_{2.5}$  concentrations over CEC. Most of OBB contributions were dominated by OCSB, especially in Henan, Anhui,  
Hubei, and Hunan, while other types of OBB emissions also exerted certain influence in Jiangxi, Zhejiang, and Fujian. With  
55 the concentration-weighted trajectory (CWT) method, potential OCSB sources leading to severe haze in Henan, Anhui,  
Hubei, and Hunan were pinpointed. The results illustrated that the OCSB emissions in Henan and Anhui can cause haze not  
only locally but also regionally through regional transport. Combining with meteorological analyses, we can find that surface  
weather patterns played a cardinal role in reshaping spatial and temporal characteristics of  $PM_{2.5}$  concentrations. Stationary  
high-pressure systems over CEC enhanced local  $PM_{2.5}$  concentrations in Henan and Anhui. Then, with the evolution of  
60 meteorological patterns, Hubei and Hunan in the low-pressure system were forced to receive the pollution from areas (i.e.,  
Henan and Anhui) enveloped in the high-pressure system. These results highlight that policymakers should strictly undertake  
interprovincial joint enforcement actions to prohibit irregular OBB, especially OCSB over CEC. By comparison, the  
constrained OBB emissions can, to a large extent, not only supplement insufficient estimations derived from satellite  
retrievals but also reduce overestimations of bottom-up methods.



## 65 **1 Introduction**

Open biomass burning (OBB) has adverse impacts on ambient air quality and human health, owing to the fact that OBB generally emits abundant gaseous and particulate pollutants in a short period of time, particularly carbonaceous aerosols (e.g., black carbon (BC) and organic carbon (OC)) (Li et al., 2010; Rose et al., 2010; Cheng et al., 2013; Ding et al., 2013; Cheng et al., 2014; Saleh et al., 2014; Washenfelder et al., 2015; Vakkari et al., 2018; Bikkina et al., 2019). It has been estimated that OBB contributes approximately 65 % of global annual average primary OC emissions (Bond et al., 2013), and more than 40 % of fine particulate matter (PM<sub>2.5</sub>) concentrations in specific cases of regional haze (Zhang and Cao, 2015; Long et al., 2016; Gao et al., 2016; Sun et al., 2016; Li et al., 2017). In China, estimated growth rates of BC, OC and primary PM<sub>2.5</sub> emitted by OBB from 2002 to 2016 were 180 %, 191 %, and 192 %, respectively (Mehmood et al., 2018), suggesting an urgent need to control OBB emissions.

Open crop straw burning (OCSB), as a crucial part of OBB, generally occurs on a large spatial scale during the harvest seasons in regions with intensive agriculture activities, because it is still the most effective, efficient and economical measure to dispose of open crop straw (Li et al., 2007; Qin and Xie, 2011; Zhang et al., 2017; Zhuang et al., 2018; Xu et al., 2019; Zhang et al., 2019). Previous studies illustrated that air pollutant emissions from OCSB accounted for more than 80% of those from OBB over China during the past decade. More importantly, emissions increased steadily during the past decade, thereby directly causing or substantially exacerbating regional haze (Wu et al., 2018).

China is experiencing frequent and severe regional haze, partly resulting from substantial and extensive OBB (Bi et al., 2010; Huang et al., 2014; Andersson et al., 2015; Zhang et al., 2015; Zhang et al., 2015a; Hong et al., 2016; Chen et al., 2017; An et al., 2019). Open crop straws in China accounted for around 20 % of global production and rose with the average annual rate of 4 % during the past decade (Bi et al., 2010; Hong et al., 2016). Specifically, central and eastern China (CEC), as a cardinal granary in the world, was associated with large quantities of crop planting and thus played a crucial role in intensive OCSB, which has been suspected of causing rapid increases of PM<sub>2.5</sub> concentrations in this region during the harvest seasons (Yamaji et al., 2010; Wang et al., 2015; Zhang et al., 2016; Ding et al., 2016; Liu et al., 2018; Wang et al., 2018; Yu et al., 2019). Therefore, it is necessary to understand the effects of OBB and OCSB on haze formation over CEC in order to provide effective regulations on mitigating OBB activities.

Current studies indicate, however, that high uncertainties exist in accurately quantifying impacts of OBB on a regional scale using chemical transport models (CTMs). This arises from two major reasons. First is the challenge of representing the magnitude and spatiotemporal distribution of OBB and OCSB emissions, despite the emergence of newly developed OBB emission inventories during the past decade (Streets et al., 2003; Liu et al., 2015; Zhang and Cao, 2015; Zhang et al., 2015a; Li et al., 2016; Qiu et al., 2016; Zhou et al., 2017; Zhao et al., 2017; Liu et al., 2018a; Liu et al., 2018b; Zhang et al., 2019; Dai et al., 2019). This is mainly because traditional bottom-up statistical methods cannot capture rapid outbreaks of OBB and OCSB and fail to produce reliable emission amounts and distributions. Moreover, few studies applied CTMs to evaluate these bottom-up emissions. Also, satellite-based top-down emission inventories cannot generally resolve small fire hotspots



(usually around large ones) and can underestimate OBB and OCSB emissions by 2 ~ 20 times (Wiedinmyer et al., 2011; Randerson et al., 2012; Uranishi et al., 2019). Several studies have attempted to improve the performance of CTMs by increasing OBB or OCSB emissions with a uniform proportion regardless of specific spatial and temporal scales (Chuang et al., 2015; Pimonsree et al., 2018; Uranishi et al., 2019). Recent studies used observed and simulated constraints to optimize OBB emissions (Hooghiemstra et al., 2012; Konovalov et al., 2014; Yang and Zhao, 2019). Nevertheless, this method still did not represent the spatiotemporal heterogeneity of uncertainties in OBB emissions and has never been used in CEC. Therefore, the constraining method combining sufficient observed and simulated results, as well as satellite-based fire information, could provide the prospective alternative to optimize OBB emissions. To support related policy-making more effectively, potential major OBB emission sources and corresponding meteorological drivers should also need to be identified.

Instantaneous emissions from OBB and OCSB are also poorly co-constrained because of the difficulty of distinguishing their measurements simultaneously with high spatial and temporal resolution (Yan et al., 2006; Tsao et al., 2012; Lei et al., 2013; Zhang et al., 2013; Cheng et al., 2013; Monks et al., 2015; Laing et al., 2016; Chen et al., 2017; Wu et al., 2018; Hamilton et al., 2018; Lee et al., 2018; Li et al., 2019; Uranishi et al., 2019; Yang and Zhao, 2019). Consequently, most of the previous studies focused only on individual biomass (e.g., corn, wheat, and rice) or total OBB. Hence, few findings could isolate spatial and temporal influences of OCSB from those of OBB in China, especially over CEC (Li et al., 2007; Cao et al., 2008; Fu et al., 2012; Cheng et al., 2014; Huang et al., 2014; Long et al., 2016; Zhang et al., 2019). Satellite observations by NASA's moderate resolution imaging spectroradiometer (MODIS) or visible infrared imaging radiometer (VIIRS) offer an attractive alternative by providing fire information (e.g., burned areas, fire locations) that is able to distinguish OCSB from total OBB. Further, these observations can derivatively serve as the computational basis to yield products for their respective emissions, such as the Fire INventory from NCAR version 1.5 (FINNv1.5) (Wiedinmyer et al., 2011).

Comprehensive quantitative analyses of relative effects of OBB and OCSB on haze formation is of critical significance for CEC. In this study, we focus on June in 2014, when abundant  $PM_{2.5}$  with exceptionally high concentrations (e.g., the hourly peak surface  $PM_{2.5}$  concentration  $> 200 \mu g m^{-3}$ ) enveloped the CEC, potentially due to effects of intense OBB and OCSB emissions during this harvest season. To understand the evolution of regional haze over CEC, we analyzed spatial and temporal characteristics in the OBB and OCSB emissions in FINNv1.5, ground-measured  $PM_{2.5}$  concentrations, and satellite-based aerosol optical depth (AOD). We have established a constraining method that integrates abundant ground-level  $PM_{2.5}$  measurements with a state-of-art fully coupled regional meteorological and chemical transport model (i.e., the two-way coupled WRF-CMAQ) in order to derive optimal OBB emissions based on the original FINNv1.5 emissions. With these constrained emissions, the model reproduced spatiotemporal variations in chemical and meteorological fields well. Further, we applied the model to simultaneously quantify the relative contributions of OCSB and OBB emissions to surface  $PM_{2.5}$  concentrations. The backward trajectory (HYSPLIT) and concentration-weighted trajectory (CWT) methods were integrated to pinpoint potential major OCSB sources. Corresponding meteorological patterns resulting in this regional haze event were also analysed. Finally, we compare the constrained OBB emissions as well as their associated effects with previous studies.



## 2 Methods and data

### 2.1 The two-way coupled WRF-CMAQ model

We utilize the two-way coupled Weather Research and Forecasting (WRF) model and Community Multiscale Air Quality (CMAQ) model (i.e., the two-way coupled WRF-CMAQ model, hereinafter as the WRF-CMAQ model) (Wong et al., 2012; Yu et al., 2013) to simulate meteorological and chemical fields over CEC (Yu et al., 2018). This fully-coupled model represents a significant advancement over the offline WRF-CMAQ system (Byun and Schere, 2006). That is mainly because the former expands to encompass aerosol-radiation interactions to which OBB and OCSB should be closely related (Wang et al., 2014; Huang et al., 2016; Baró et al., 2017; Li et al., 2017b; Singh et al., 2018; Malavelle et al., 2019). In addition, the newly developed coupler helps to improve the consistency between WRF and CMAQ with regard to meteorological characteristics (Wong et al., 2012).

The WRF-CMAQ model was configured with the CB05 and AERO6 schemes for gas and aerosol chemistry simulations, respectively (Yarwood et al., 2005; Carlton et al., 2010); thus primary emissions (e.g., primary OC, BC, and dust) and secondary pollutants (e.g., secondary sulfate, nitrate, ammonium, and organic aerosols) are both considered. The classification of aerosols is described by three modes (Aitken, Accumulation, and Coarse) with a lognormal distribution (Seinfeld and Pandis, 2016). Additionally, the ISORROPIA II model was applied to perform thermodynamic equilibrium calculations for  $K^+-Ca^{2+}-Mg^{2+}-NH_4^+-Na^+-SO_4^{2-}-NO_3^- -Cl^- -H_2O$  aerosol systems among gas, liquid and particulate phases (Fountoukis and Nenes, 2007). In terms of meteorology simulations, we selected the two-moment Morrison cloud microphysics scheme (Morrison and Gettelman, 2008), the Kain-Fritsch cumulus cloud parameterization scheme (KF2) (Kain, 2004), the Rapid Radiative Transfer Model for General circulation models (RRTMG) (Clough et al., 2005), the Pleim-Xiu land surface scheme (PX) (Xiu and Pleim, 2001) and the asymmetric convective model (ACM2) (Pleim, 2007a; Pleim, 2007b) for the cloud physics, radiative transfer, land surface energy balance and planetary boundary layer simulations, respectively.

Meteorological initial and lateral boundary conditions were derived from the ERA interim reanalysis dataset operated by the European Centre for Medium-Range Weather Forecasts (ECMWF) with spatial resolution of  $1^\circ \times 1^\circ$  and temporal resolution of 6 hours (<http://www.ecmwf.int/products/data>, last access: 2 August 2019). The CMAQ-default initial and boundary chemical conditions were used. A spin-up period of seven days was used to minimize the influence of initial chemical conditions (Liu et al., 2010; Wang et al., 2012; Liu et al., 2018b). To eliminate numerical artifacts that commonly occur in WRF external boundary relaxation zones, we trimmed off seven grid cells on each edge of the domain (Wong et al., 2012; Yu et al., 2012). In addition, meteorological fields were reinitialized by reanalysis data every 48 hours in order to constrain corresponding simulated results (Lo et al., 2008; Zhao et al., 2010; Zhang et al., 2016b).

In this study, the Multi-resolution Emission Inventory for China version 1.2 (MEICv1.2) (<http://www.meicmodel.org>, last access: 2 August 2019) mainly implemented by Tsinghua University was used for anthropogenic emissions (Li et al., 2015a). This inventory comprises five anthropogenic sectors (i.e., industry, power plants, residential and transport and agriculture)



165 for  $PM_{2.5}$  and its major precursors (e.g., CO, SO<sub>2</sub>, NO<sub>x</sub>, primary  $PM_{2.5}$ ). It also builds a framework to speciate the non-  
methane volatile organic compounds (NMVOCs) and further establish model-ready NMVOC emissions in accordance with  
the CB05 mechanism. Anthropogenic emissions outside China were derived from the Task Force Hemispheric Transport of  
Air Pollution version 2 (HTAPv2) (Janssens-Maenhout et al., 2015; Li et al., 2017b), which includes two additional sectors  
(i.e., aircrafts and ships). These two additional sectors were then aggregated to the transport sector so as to remain  
170 compatible with MEICv1.2 with regard to anthropogenic sectors. Unlike off-line anthropogenic emissions, natural sources  
for biogenic and dust emissions were calculated inline using the Biogenic Emission Inventory System version 3.14  
(BEISv3.14) (Carlton and Baker, 2011) and a windblown dust scheme embedded in CMAQ (Choi and Fernando, 2008),  
respectively.

To examine OBB and OCSB impacts over CEC, we conducted the simulations in a domain covering most of China with a 12  
175 km horizontal resolution (Fig. 1). There were 31 sigma-pressure vertical layers ranging from the surface to the top pressure  
of 100 hPa, 20 of which are located below around 3 km to achieve finer meteorological and chemical characteristics within  
the planetary boundary layer. It should be noted that CEC in this study comprises 10 provinces, including Anhui (AH),  
Hubei (HB), Henan (HEN), Hunan (HUN), Shandong (SD), Zhejiang (ZJ), Jiangsu (JS), Shanghai (SH), Fujian (FJ) and  
Jiangxi (JX), which are underlined with black thick outlines in Fig. 1.

## 180 2.2 OBB and OCSB emissions

In this study, we used FINNv1.5 to characterize spatiotemporal features of OCSB and other types of OBB emissions.  
FINNv1.5 provides an unique chance to characterize spatial and temporal estimations of trace gas and particle emissions  
from seven types of OBB, including savannas, grasslands, woody savannas, shrublands, tropical forests, temperate forests,  
boreal forests, and croplands (Wiedinmyer et al., 2011). Its distinctive advantages include global coverage, high temporal  
185 and spatial resolutions (daily and 1km), and adequate land use types, mainly due to the utilization of MODIS NRT active fire  
products (MCD14DL, <https://firms.modaps.eosdis.nasa.gov>, last access: 5 August 2019), which are processed with the  
standard MOD14/MYD14 fire and thermal anomalies. Nevertheless, several critical weaknesses originating from satellite  
retrievals are present, as mentioned above. Thus, the corresponding OBB emissions are prone to be largely underestimated  
(Chuang et al., 2015; Pimonsree et al., 2018; Uranishi et al., 2019). Some previous studies indicated that the actual total  
190 amount of primary  $PM_{2.5}$  emissions over Northeast China was nearly 20 times higher than that estimated by FINNv1.5  
(Uranishi et al., 2019). Additionally, the lack of local emission information (e.g., local biomass loading data, emission  
factors) could introduce extra uncertainties. Therefore, FINNv1.5 utilized in this study should require further adjustments to  
achieve more accurate estimates for OBB and OCSB emissions.

It is important to represent injection heights of OBB in CTMs, which could significantly affect its regional transport.  
195 Previous studies demonstrated that different injection heights could lead to distinct  $PM_{2.5}$  responses (Freitas et al., 2006;  
Leung et al., 2007) and pressure-weighted injections within the troposphere is a reliable alternative (Hyer et al., 2007). In  
this study, we determined heights of the hourly top ( $P_{top}$ ) and bottom ( $P_{bottom}$ ) of the OBB plume using a quick plume rise



model (Eq. (1) and Eq. (2)) based on the buoyant efficiency ( $B$ ) available from the corresponding hourly and size class tables (Tai et al., 2008; Fu et al., 2012a) as follows:

$$200 \quad P_{top} = (B_{hour})^2 \times (B_{size})^2 \times P_{topmax}, \quad (1)$$

$$P_{bottom} = (B_{hour})^2 \times (B_{size})^2 \times P_{bottommax} \quad (2)$$

where  $P_{topmax}$  and  $P_{bottommax}$  are parameters that define the potential max plume heights for  $P_{top}$  and  $P_{bottom}$ , respectively.

### 2.3 Analysis of backward trajectories and concentration-weighted trajectories

The Hybrid Single-Particle Lagrangian Integrated Trajectory version 4 (HYSPPLIT4) model developed by National Oceanic  
205 and Atmospheric Administration Air Resources Laboratory (NOAA ARL) was employed to predict regional transport pathways arriving at receptor cities of interest (Stein et al., 2015). HYSPPLIT4 was driven by the final global meteorology analysis data obtained from the National Centers for Environmental Prediction's Global Data Assimilation System (<https://ready.arl.noaa.gov/archives.php>, last access: 5 August 2019) with a  $1^\circ \times 1^\circ$  latitude–longitude grid, and was run four times per day at starting times (i.e., 00:00, 06:00, 12:00 and 18:00 LT) with the starting height of 100 m above ground level.  
210 In this study, the 48 h back trajectories of air masses were used for further analyses. More details about the HYSPPLIT4 model can be found at <http://www.arl.noaa.gov/ready/open/hysplit4.html> (last access: 2 August 2019).

We adopted the concentration-weighted trajectory (CWT) method to pinpoint potential major OBB sources affecting regional surface  $PM_{2.5}$  concentrations during the study period based on above HYSPPLIT analysis and surface  $PM_{2.5}$  observations (Wang et al., 2009; Yu et al., 2014; Li et al., 2015b). The CWT method collected all concentrations of  
215 trajectories in an individual grid ( $C_i$ ) to calculate the corresponding average CWT value ( $C_{ij}$ ) for each grid cell ( $i, j$ ) by the following Eq. (3) (Hsu et al., 2003):

$$C_{ij} = \frac{1}{\sum_{l=1}^M T_{ijl}} \sum_{l=1}^M C_l T_{ijl}, \quad (3)$$

where  $l$  and  $M$  denote the index and the total number of the trajectories, respectively, and  $T_{ijl}$  represent the residence time for the trajectory  $l$  spent in the grid ( $i, j$ ). The relatively higher CWT values imply high potential contributions to elevated  $PM_{2.5}$   
220 values at the receptor site. Thus, the weighted concentration fields can be utilized to determine the relative significance of potential sources for regional haze in CEC.

### 2.4 Observational data

The hourly mass concentrations of surface  $PM_{2.5}$  and other chemical species (i.e., CO, NO<sub>2</sub>, SO<sub>2</sub>, O<sub>3</sub>, and PM<sub>10</sub>) were continuously measured by the Ministry of Ecological Environment of China (<http://www.cnemc.cn/>, last access: 2 August  
225 2019), including 340 monitoring sites in 65 cities during the study period over CEC. These monitoring data were used to accomplish four tasks. (1) According to the evolution of surface  $PM_{2.5}$  concentrations over CEC, we can characterize changes in spatial and temporal patterns of regional haze induced by OBB. (2) We compared simulated chemical and



meteorological fields with surface observations to evaluate model performance. (3) The data were used to estimate potential sources by the CWT method. Daily mean values of AOD at 550 nm retrieved from multiple satellite platforms were examined during the target period to highlight significant spatial and temporal variabilities of regional haze in CEC. Here episode-averaged AOD products from MODIS (MOD08\_D3) at 550 nm and OMI (OMERUVd v003) at 500 nm were both utilized (<https://giovanni.sci.gsfc.nasa.gov/giovanni/>, last access: 5 August 2019).

To present OBB and OCSB emissions, daily fire products generated by MODIS (MCD14DL) and corresponding emissions were collected to exhibit explicit spatial and temporal evolutions of OBB. Along with the HYSPLIT4 and CWT method, integrated analyses of surface weather patterns from the Korea Meteorological Administration (<http://www.kma.go.kr/eng/weather/images/analysischart.jsp>) were conducted to illustrate meteorological fields triggering the regional haze over CEC.

### 3 Results and discussion

#### 3.1 OBB and OCSB information in FINNv1.5

We collected monthly OCSB and other types of OBB information estimated by FINNv1.5 over CEC throughout 2014. From the perspective of the monthly variation in numbers of fire hotspots (Fig. 2), total OBB exhibited a notable seasonal pattern with one distinct peak in summer, especially in June (19 % of the yearly total value). We further examined each type of OBB classified by seven land use categories (i.e., Croplands, Grass land/savanna, Woody savanna/shrublands, Tropical forest, Temperate forest, Boreal forest, and Temperate evergreen forest) and found that the relative contribution of OCSB ranged from 13 % to 86 % and also peaked in June of 2014. This presented a highly consistent trend with that of OBB, indicating that OCSB might be the leading contributor of OBB sources over CEC. Therefore, to simultaneously investigate OCSB and other types of OBB effects over CEC, June 2014 should be the best target period on which to focus.

Figure 3 shows a remarkable variation in spatiotemporal distributions of daily OCSB and other types of OBB fire hotspots over CEC from June 1 to 19, exhibiting a complete OBB evolutionary process. An OBB outbreak event occurred from June 5 to 14 with the maximum number of fire hotspots (more than 800). To the contrary, there existed much fewer fire hotspots in the other periods. Hence this period can, in turn, be divided into the following three episodes: EP1 (from June 1 to 4), EP2 (from June 5 to 14) and EP3 (from June 15 to 19), which represented the pre-OBB, OBB and post-OBB stages, respectively. It should be noted that OCSB makes uniformly much larger relative contributions to total OBB than other types in terms of the number of fire hotspots for the study period with more than 80 % during EP2.

During EP1 and EP3, limited OBB fire hotspots were sparsely distributed over CEC, as shown in Fig. 3. For the period of the OBB outbreak (EP2), most of the OCSB fire hotspots concentrated in Henan (32 %) and Anhui (41 %), where thereby local OCSB emissions might play a key role in shaping spatiotemporal distributions of  $PM_{2.5}$  concentrations. Owing to regional transport, surrounding areas, such as Hubei, Hunan, and Jiangxi, might be significantly influenced by OCSB, depending on meteorological conditions. The activity levels of other types of OBB during EP2 also increased by 250 %



260 compared to normal situations, particularly in Anhui, Zhejiang, and Jiangxi, although it was still significantly lower than those of OCSB, as indicated in Fig. 3.

Table S1 summarizes original provincial emissions of gaseous and particulate species for OCSB and total OBB during the study period based on the FINNv1.5 emission estimations. Most (85 %) of OBB emissions came from those occurring during EP2. As expected, OCSB dominated OBB emissions (74 % ~ 94 %) by totally producing 3040, 17, 10781, 367, and 399 million moles of NMVOCs, SO<sub>2</sub>, CO, NH<sub>3</sub>, and NO<sub>x</sub>, respectively, and 1877, 8977, 15778, 19097 tons of EC, OC, primary PM<sub>2.5</sub> and PM<sub>10</sub>, respectively. During EP2, Henan and Anhui were the top two contributors over CEC and totally accounted for 66 ~ 76 % of OBB emissions. Specifically, from the perspective of total OBB emissions in Henan and Anhui, OCSB emissions in these two provinces contributed 94 % of NMVOCs, 72 % of SO<sub>2</sub>, 87 % of CO, 88 % of NH<sub>3</sub>, 90 % of NO<sub>x</sub>, 89 % of EC, 76 % of OC, 74 % of PM<sub>2.5</sub> and 75 % of PM<sub>10</sub>, respectively. Other types of OBB emissions mainly occurred in Anhui  
265  
270 (29 %), Zhejiang (28 %) and Jiangxi (14 %). It should be pointed out that OBB emissions mainly associated with OCSB estimated in the original FINNv1.5 were projected to be substantially underestimated due to a variety of satellite-based limitations, such as unresolved small and ephemeral agricultural fires, occlusion effects of prevalent cloud cover, or discontinuous time spans (Streets et al., 2003; Wiedinmyer et al., 2011; Randerson et al., 2012; Zhou et al., 2018; Uranishi et al., 2019).

### 275 3.2 Characteristics of observed regional haze pollution

Both ground and space observations were used to diagnose this OBB event and its associated regional haze (Fig. 4, 5, and 6). Figure 4 shows the magnitudes and spatial distributions of observed episode-averaged PM<sub>2.5</sub> concentrations over CEC for EP1, EP2, and EP3. Before the OBB outbreak (EP1), there were no extreme PM<sub>2.5</sub> concentrations, all of which were generally lower than 75 µg m<sup>-3</sup>. For EP2, elevated PM<sub>2.5</sub> concentrations (> 115 µg m<sup>-3</sup>) were observed in Henan and Anhui.  
280 Apparently, this was highly consistent with spatiotemporal distributions of OCSB (Fig. 3), which was thus anticipated to cause potential prominent impacts on local haze formation. On the other hand, regional haze also occurred in Hubei and Hunan, where no extensive high-intensity OCSB emissions were observed during the study period (Fig. 3). This means that not only OCSB emissions but also regional transport played a key role in giving rise to regional haze. It should be noted that limited emissions from other types of OBB also have a certain impact. With the sudden decline in OBB and PM<sub>2.5</sub> concentrations over CEC during EP3, however, moderate regional haze (PM<sub>2.5</sub> concentrations >75 µg m<sup>-3</sup>) lingered in Henan and Anhui. In addition to a certain degree of anthropogenic contributions, this phenomenon is probably due to unfavorable meteorological conditions, which trapped previously generated emissions during EP2.

Figure 5 shows spatial distributions of episode-averaged AOD observed by MODIS (MOD08\_D3) at 550 nm and OMI (OMERUVd v003) at 500 nm during EP2. They are in good agreement with each other and spatial distributions of surface average PM<sub>2.5</sub> concentrations. For instance, much higher AOD values were mostly detected in Henan, Anhui, Hubei, and Hunan, associated with relatively high surface observed PM<sub>2.5</sub> concentrations and substantial OCSB emissions as shown in Figs. 3 and 4. In addition, both satellite-based products detected that spatial distributions of high AOD values covered wider  
290



areas than the ground measurements, such as in Jiangxi, Zhejiang and Fujian. This was possibly due to the fact that PM suspended in the upper troposphere was more easily transported than that on the ground. This phenomenon further illustrates that OBB dominated by OCSB is not only a significant local pollution source but also an important regional pollution source. Collectively, seven provinces (i.e., Henan, Anhui, Hubei, Hunan, Jiangxi, Zhejiang, and Fujian) are the focal areas affected by OBB. To further understand the evolution of regional haze characteristics, we focused on these seven provinces to analyze time series of provincial hourly  $PM_{2.5}$  concentrations during the study period (Fig. 6). Correspondingly, the observed trends were also divided into three distinct stages on the basis of  $PM_{2.5}$  concentrations. For EP1, hourly  $PM_{2.5}$  concentrations over CEC were relatively low and almost never exceeded  $75 \mu\text{g m}^{-3}$ . Specifically, the average values in these seven provinces during this episode were  $50 \mu\text{g m}^{-3}$ ,  $59 \mu\text{g m}^{-3}$ ,  $71 \mu\text{g m}^{-3}$ ,  $65 \mu\text{g m}^{-3}$ ,  $44 \mu\text{g m}^{-3}$ ,  $46 \mu\text{g m}^{-3}$ , and  $41 \mu\text{g m}^{-3}$ , respectively, depicting a period with a relatively clean air environment. For EP2 with the OBB outbreak mainly associated with OCSB,  $PM_{2.5}$  concentrations increased significantly in most of these provinces, and the mean  $PM_{2.5}$  concentrations in these seven provinces could reach values of  $135 \mu\text{g m}^{-3}$ ,  $175 \mu\text{g m}^{-3}$ ,  $182 \mu\text{g m}^{-3}$ ,  $147 \mu\text{g m}^{-3}$ ,  $129 \mu\text{g m}^{-3}$ ,  $72 \mu\text{g m}^{-3}$ , and  $37 \mu\text{g m}^{-3}$ , respectively. This indicates the extensive haze in Henan, Anhui, Hubei and Henan. For Jiangxi and Zhejiang during EP2, no severe haze was detected despite large increases in  $PM_{2.5}$  concentrations relative to those in EP1. Thereafter,  $PM_{2.5}$  concentrations in most parts of CEC decline rapidly and gradually stabilize in a lower range during EP3. Overall, the spatiotemporal evolution trends of regional haze characteristics were highly related to those of OBB emissions as analyzed above, signifying the dominant role of OBB emissions. As shown in these results, there were two important issues, which should be identified. (1) The temporal variations in  $PM_{2.5}$  concentrations in Hubei were highly similar to those in Hunan during the target period, especially in EP2, revealing that coincident unfavourable meteorological fields might facilitate severe haze there. (2) Relative to the evolution of regional haze in Henan, there was a distinct time lag (24 h ~ 48 h) for those in Hubei and Hunan. This indicates that OBB emissions mainly associated with OCSB in Henan as well as subsequent regional transport might also be responsible for severe haze in Hubei and Hunan.

In conclusion, from the point of view of the highly correlated evolution relationship between regional haze and OBB activities, we can infer that OBB mainly associated with OCSB might dominate spatial and temporal variations in relatively high  $PM_{2.5}$  concentrations over CEC, especially in Henan, Anhui, Hubei, and Henan during the study period. Besides, meteorological fields should also play a critical role in shaping spatiotemporal variations in the regional haze, whereas other types of OBB emissions might be responsible for local haze in Zhejiang and Jiangxi. Therefore, relative contributions of OCSB and other types of OBB, as well as relevant meteorological fields, to regional haze formation at different regional scales are not consistent and should be accurately examined.

### 3.3 Constrained optimal OBB emissions

Given large uncertainties in the OBB emissions estimated by the original FINNv1.5, it is necessary to refine these emissions in order to allow the WRF-CMAQ model to reproduce the magnitudes and spatiotemporal distributions of regional haze induced by this OBB event. Also, it is the prerequisite to accurate estimations of OCSB and other types of OBB



contributions. In this study, all available observations from 340 ground monitoring sites and the WRF-CMAQ model simulations were used in co-constraining OCSB and other types of OBB emissions from FINNV1.5. This constraining method contained two steps: (i) To characterize the nonlinearity between emissions and  $PM_{2.5}$  concentrations, we examined model responses to variable OBB emission perturbations, which referred to variably amplifying OBB emissions using coefficients arranged in an arithmetic sequence (Xiao et al., 2010; Digar and Cohan, 2010; Tang et al., 2011), whose first term was 1, being consistent with the constant difference of terms; (ii) Subsequently, simulated  $PM_{2.5}$  concentrations were then compared with available observations. Hence, with variable emission perturbations, this evaluation process would be repeated, and simulated results could gradually approach observations. During the evaluation processes, the normalized mean bias (NMB) was selected as the major indicator to characterize the discrepancy (Yu et al., 2006).

The constraining method took consideration of the spatiotemporal heterogeneity of uncertainties in OBB emissions to derive the optimal adjustment coefficients for OBB emissions more accurately. According to the variations in the OBB activity level, as shown in Fig. 3 and Table S1, the entire study period was divided into three periods, as noted before, i.e., the pre-OBB (EP1), OBB (EP2) and post-OBB (EP3) stages. Nevertheless, in terms of regional haze, only EP1 was treated as the normal situation under the consideration that  $PM_{2.5}$  concentrations during EP3 would be inevitably impacted by residual emissions produced by this OBB event during EP2. To eliminate potential uncertainties in other emission sources (i.e., anthropogenic and biogenic emissions), we evaluated the model capability under normal situations (no OBB event), that is, the model was driven by original OBB emissions as well as anthropogenic and biogenic emissions (referred to as the BASE case). Figure 6 illustrates the simulated provincial average  $PM_{2.5}$  concentrations in the BASE case during the study period for Henan, Anhui, Hubei, Hunan, Jiangxi, Zhejiang, and Fujian. The results show that the model uniformly underestimated observations during the study period. However, the NMBs were within a reasonable range ( $> -25\%$ ) during EP1 but presented much lower values ( $> 40\%$ ) during the rest periods. Thus, this demonstrates that original OBB emissions as well as other sources can allow the model to capture spatiotemporal variations in  $PM_{2.5}$  concentrations for normal situations without significant impacts of OBB in most of provinces, as recorded by previous studies (Hu et al., 2015; Liu et al., 2016; Qiao et al., 2019), whereas the model failed to reproduce the rapid outbreak of  $PM_{2.5}$  concentrations for this OBB event, especially during EP2 in Henan and Anhui. These results confirmed that the model can have reasonable estimates of OBB emissions for normal situations (i.e., EP1) but significant underestimations of those for this OBB event. This result shows the need to derive optimal OBB emissions using this constraining method. On the other hand, for EP1, we also need to overcome slight underestimations of simulated  $PM_{2.5}$  concentrations in order to improve model performance and subsequent estimates of OBB contributions.

Based on the comprehensive analyses for OBB emissions and their associated regional pollution, our purpose here is to extend this constraining method to specific spatiotemporal scales. This means that the three study stages (EP1 ~ EP3) should be discriminated due to their distinct OBB emissions, namely, different coefficients should be adopted to adjust OBB emissions for each individual study period. As discussed in Sections 3.1 and 3.2, Henan and Anhui were the top two provinces that contributed local OBB emissions ( $> 80\%$ ) during the entire study period and would affect other provinces



360 through regional transport. Hence three areas (Henan, Anhui, and other provinces over CEC) were selected as separate  
adjustment objects in their turn as shown in Fig.7. Therefore, to accomplish this purpose, we need to employ this  
constraining method in the following ways: (i) derive respective optimal OBB emissions in Henan and Anhui for EP1 at first  
and then for EP2. Note that the optimal adjustment coefficient for EP1 would also be appropriate for EP3 due to the fact that  
both of them represent the normal situation with respect to the OBB emissions; (ii) on the basis of those results, the next step  
365 was to derive corresponding optimal OBB emissions for other provinces.

Figure 7 exhibits colored cells to represent NMBs between observed and simulated  $PM_{2.5}$  concentrations that characterize  
model responses to variable OBB emission perturbations in Henan, Anhui, and other provinces over CEC. The numbers on  
the X and Y axes refer to the adjustment coefficients for OBB emissions for EP1 and EP2, respectively. With variable OBB  
emission perturbations, simulated results gradually approached to observed values. For Henan and Anhui, OBB emissions  
370 with relatively low adjustment coefficients (1 ~ 5) cannot allow the model to capture observed high  $PM_{2.5}$  concentrations  
during EP2, while those with higher adjustment factors ( $> 4$ ) would cause the model to significantly overestimate observed  
values during EP1. This phenomenon highlights the substantial underestimation of original OBB emissions in FINNv1.5,  
especially during the OBB outbreak period (i.e., EP2). By comparison, relatively low coefficients should be adopted to  
adjust OBB emissions in other provinces. These results point to the importance of variable emission perturbations by  
375 considering the spatiotemporal heterogeneity in optimizing OBB emissions. Specifically, we can finally determine that  
optimal coefficients for OBB emissions for Henan, Anhui, and other provinces were 6, 7, and 4 for EP2, respectively, and 4,  
4, and 2 for both EP1 and EP3, respectively. Correspondingly, all of the NMB values reached the minimum and were  
controlled within  $\pm 5\%$ . In summary, we would employ the aforementioned optimal coefficients to adjust OBB emissions at  
specific spatiotemporal scales. Table 1 summarizes the spatiotemporal emission amounts for all the species (NMVOCs,  $SO_2$ ,  
380  $CO$ ,  $NH_3$ ,  $NO_x$ , EC, OC,  $PM_{2.5}$ ,  $PM_{10}$ ) for each province over CEC for each stage of the study period (EP1 ~ EP3).  
Corresponding maps of  $PM_{2.5}$  emissions for OCSB and other types of OBB presented similar spatial distributions to those of  
fire hotspots as shown in Fig. 8. By taking  $PM_{2.5}$  emitted from OCSB as an example, emission intensities in some pixels  
were found to exceed a value of 100 tons during the study period, and most cases were found in the areas surrounding the  
common border of Henan and Anhui. For other provinces,  $PM_{2.5}$  emission intensity only ranged from 1 to 20 tons per pixel.  
385 Other species from OCSB emissions presented similar spatial distributions. On the other hand, all species for other types of  
OBB consistently showed sparse spatial distributions and limited emissions.

In summary, the optimal OBB emissions were derived by the constraining method which integrated observations and model  
results based on FINNv1.5. Note that this constraint was established based on specific spatial scales separately (i.e., Henan,  
Anhui, and rest provinces over CEC). Therefore, due to the nonlinearity between emissions and  $PM_{2.5}$  concentrations, the  
390 accuracy of the optimal OBB emissions should be extrapolated to the entire CEC in order to verify the model reliability.



### 3.4 Model evaluation

Accurate simulations of meteorological and chemical fields were prerequisite to precise estimations of OBB contributions to the haze formation. Few previous OBB emissions established by bottom-up or top-down methods were evaluated directly. Here we assessed the optimal OBB emissions with the WRF-CMAQ model by evaluating its performance. This case is abbreviated as the OPT case hereinafter. The simulated chemical species (i.e.,  $PM_{2.5}$ ,  $O_3$ ,  $SO_2$ ,  $CO$ , and  $NO_2$ ) and meteorological parameters (i.e., 10 m wind speed and direction, 2 m temperature, and PBLH) from the model were both taken into considerations by comparing with ground observations.

Figure 4 illustrates spatial distributions of observed and simulated hourly  $PM_{2.5}$  concentrations in the OPT case for the entire CEC in EP1, EP2, and EP3. As discussed in Section 3.3, the OBB emissions from FINNv1.5 can drive the model to achieve reasonable results for normal situations, such as EP1, which, however, remained to be slight underestimations of observations. It is important to note that the simulated  $PM_{2.5}$  concentrations in the BASE case were significantly lower than observations at most of monitoring sites during EP2, especially in Henan, Anhui, Hubei, and Hunan as mentioned before. This implies that the original OBB emissions from FINNv1.5 substantially underestimate the emissions during the period of the OBB outbreak (i.e., EP2). Compared to the BASE case, the model results in the OPT case were able to reproduce the magnitudes and spatial patterns of observed  $PM_{2.5}$  concentrations much better. Specifically, the model with the optimal OBB emissions can not only capture extremely high observations ( $> 115 \mu g m^{-3}$ ) in Henan, Anhui, Hubei, and Hunan for the OBB event during EP2, but also succeeded in reproducing relatively lower values in other provinces at the same time. For EP1 and EP3, simulated results in the OPT case increased to some extent as expected and became closer to observations by comparison. These results indicated reliable model performance.

To further evaluate the model performance, we examined the model capabilities at the provincial scale. Figure 6 displays the comparisons of observed and simulated hourly  $PM_{2.5}$  concentrations for the OPT case in Henan, Anhui, Hubei, Hunan, Jiangxi, Zhejiang, and Fujian. Besides the NMB, the correlation coefficient (R) was also used to evaluate the simulated results. Generally, the WRF-CMAQ model with the optimal OBB emissions can reasonably capture the temporal evolution of surface  $PM_{2.5}$  concentrations for these seven provinces. With the abundant observations as the constraint, the NMB values in these seven provinces were 1.1 %, 3.3 %, 0.2 %, 1.3 %, 1.4 %, 6.2 %, and 22.8 %, respectively, with R values of 0.90, 0.80, 0.53, 0.74, 0.56, 0.80 and 0.64, respectively. These results provide direct evidence for the reliable capability of the optimal OBB emissions, allowing the model to reproduce the steep rising curves of observed  $PM_{2.5}$  concentrations in Henan, Anhui, Hubei, and Hunan during EP2 when OBB might trigger regional haze over the central part of CEC, as shown in Figs. 4 and 6.

The first two peaks of observed  $PM_{2.5}$  during the study period occurred in Anhui and Henan. Observed  $PM_{2.5}$  concentrations in Anhui and Henan gradually increased from  $42 \mu g m^{-3}$  on June 1 to  $226 \mu g m^{-3}$  on June 7 and from  $75 \mu g m^{-3}$  on June 7 to  $226 \mu g m^{-3}$  on June 10, respectively. This phenomenon belongs to the distinct characteristics of local haze. Correspondingly, the model in Anhui and Henan can capture this general temporal pattern, especially the maximum with NMB values of 9 %



and 12 %, respectively. In contrast, regional transport might play a critical role in dominating two sudden eruptions of  
425 observed  $PM_{2.5}$  concentrations in Hubei and Hunan with relatively high values of  $335 \mu\text{g m}^{-3}$  and  $252 \mu\text{g m}^{-3}$  on June 12,  
respectively. The model to a large extent can capture these two abrupt peaks, even though consistently underestimating the  
maxima with the NMB values ranging from 20 % to -15 %. Note that there was a distinct 12 h time lag between the observed  
and simulated peaks of  $PM_{2.5}$  concentrations in Hubei, which is associated with the possible uncertainties in meteorological  
simulations.

430 For other chemical species and main meteorological parameters, Tables S2 and S3 indicate that the WRF-CMAQ model with  
the optimal OBB emissions could also reproduce reasonable results, with most R values greater than 0.7 and NMB values  
within  $\pm 30$  %. Specifically, compared to the BASE case, the NMB and R values for the species (i.e., CO,  $PM_{10}$ , and  $PM_{2.5}$ )  
greatly contributed by OBB emissions in the OPT case were also greatly improved, reaching a much better level ( $\pm 25$  %).

### 3.5 Relative contributions of OCSB and OBB to regional haze formation

435 We designed three model simulations to simultaneously isolate OCSB and OBB contributions to  $PM_{2.5}$  concentrations over  
CEC, i.e., the first with only anthropogenic and biogenic emissions (referred to as the NOBB case), the second with not only  
anthropogenic and biogenic emissions but also constrained OCSB emissions (referred to as the OPT\_OCSB case), and the  
last with not only anthropogenic and biogenic emissions but also total constrained OBB emissions (namely the OPT case). In  
this study, OCSB and OBB contributions were quantified by differences between simulated  $PM_{2.5}$  concentrations in different  
440 cases in terms of absolute mass concentrations and relative contributions as calculated in the following formulas:

$$OCSB_{\text{mass}} = OPT\_OCSB_{\text{mass}} - NOBB_{\text{mass}}, \quad (4)$$

$$OCSB_{\text{contribution}} = (OCSB_{\text{mass}} / NOBB_{\text{mass}}) \times 100 \%, \quad (5)$$

$$OBB_{\text{mass}} = OPT_{\text{mass}} - NOBB_{\text{mass}}, \quad (6)$$

$$OBB_{\text{contribution}} = (OBB_{\text{mass}} / NOBB_{\text{mass}}) \times 100 \%, \quad (7)$$

445 where  $NOBB_{\text{mass}}$ ,  $OPT\_OCSB_{\text{mass}}$  and  $OPT_{\text{mass}}$  represent simulated  $PM_{2.5}$  concentrations in the BASE, OPT\_OCSB, and  
OPT cases, respectively.  $OCSB_{\text{mass}}$  ( $OBB_{\text{mass}}$ ) and  $OCSB_{\text{contribution}}$  ( $OBB_{\text{contribution}}$ ) denote contributions from OCSB  
(OBB) with regard to absolute  $PM_{2.5}$  mass concentrations and relative contributions, respectively.

Figure 9 shows spatiotemporal distributions of  $OBB_{\text{mass}}$  and  $OBB_{\text{contribution}}$  during EP1, EP2, and EP3. For CEC, OBB  
during EP2 had much more significant impacts than those during EP1 and EP3 on regional  $PM_{2.5}$  concentrations. In  
450 particular, OBB contributed up to more than 75 % ( $> 75 \mu\text{g m}^{-3}$ ) to surface  $PM_{2.5}$  concentrations over the border of Henan  
and Anhui during EP2. These spatial distributions were exactly consistent with those of OBB emissions and the regional  
haze, implying the key role of OBB emissions in triggering the regional haze formation. In contrast,  $PM_{2.5}$  concentrations  
also increased substantially by  $14 \sim 74 \mu\text{g m}^{-3}$  ( $16 \sim 78$  %) in Hubei and Hunan, where no apparent OBB emissions were  
detected. This phenomenon should be attributed to regional transport of air pollution brought by prevalent meteorological  
455 fields. It was worth noting that, there were the substantial declines in OBB emissions and  $PM_{2.5}$  concentrations with



significant decreases in OBB contributions consistently occurring over CEC during EP3. This indicates that stringent controls on the OBB emissions were still conspicuously beneficial for regional air quality. On the other hand, massive OCSB pollutants mainly emitted in Henan and Anhui were not transported to the eastern coastal zones of CEC during EP3, because of the role of meteorology. In addition, local OBB would not lead to regional haze in the southern edge of CEC despite its large contributions ( $> 75\%$ ). As shown in Figure 10, OCSB contributions show largely similar spatiotemporal distributions to those of OBB, indicating that OCSB generally played a key role in reshaping  $PM_{2.5}$  concentrations over CEC. During the OCSB outbreak period, its relative contributions were significantly higher than those in other periods. However, OCSB contributions were located at some typical areas, namely the common border between Henan and Anhui ( $> 75\ \mu\text{g m}^{-3}$ ,  $75\%$ ) and central narrow zones between Hubei and Hunan ( $> 35\ \mu\text{g m}^{-3}$ ,  $39\%$ ). For other provinces, its relative contributions were within a narrow range of approximately  $20\%$ . Figure 11 highlights that fairly large proportions (more than  $80\%$ ) of OBB contributions came from OCSB over the most parts of CEC, indicating that OCSB should play a dominant role in reshaping spatial and temporal distributions of regional  $PM_{2.5}$  concentrations over the most parts of CEC during the study period, especially for EP2. In contrast, other types of OBB barely influenced the haze formation in Jiangxi, Fujian, and Zhejiang ( $< 10\ \mu\text{g m}^{-3}$ ).

To further understand OCSB and OBB effects on regional haze formation over CEC, time series of OBB and OCSB contributions to hourly  $PM_{2.5}$  concentrations for seven provinces over CEC during the study period are examined in Fig. 6. Overall, OBB emissions had significant contributions to hourly  $PM_{2.5}$  concentrations in Henan ( $44.14\%$ ,  $23.82\ \mu\text{g m}^{-3}$ ), Anhui ( $46.19\%$ ,  $36.24\ \mu\text{g m}^{-3}$ ), Hubei ( $56.89\%$ ,  $37.69\ \mu\text{g m}^{-3}$ ), Zhejiang ( $25.89\%$ ,  $17.79\ \mu\text{g m}^{-3}$ ), and Fujian ( $28.97\%$ ,  $7.31\ \mu\text{g m}^{-3}$ ), but lower impacts on those in Hunan ( $21.51\%$ ,  $13.86\ \mu\text{g m}^{-3}$ ) and Jiangxi ( $14.07\%$ ,  $7.11\ \mu\text{g m}^{-3}$ ). It should be noted that most of OBB ( $> 89\%$ ) contributions uniformly resulted from OCSB emissions. For the OBB outbreak period, significant OBB contributions were found in Henan ( $60.47\%$ ), Anhui ( $57.73\%$ ), Hubei ( $42.91\%$ ), and Hunan ( $29.14\%$ ), whereas those in other provinces were in a small range ( $\pm 15\%$ ), and OCSB emissions always contributed to the most (more than  $90\%$ ). Note that the variations in  $OPT\_OCSB_{\text{mass}}$  in Henan and Anhui kept generally synchronized with those in local abundant OCSB emissions and haze. In contrast, the peak values of  $OPT\_OCSB_{\text{mass}}$  in Hubei and Hunan, where no extensive fire hotspots were detected, showed apparent temporal asynchronies ( $24\text{h} \sim 48\text{h}$ ) relative to those in Henan. This means OCSB was not only one of the significant local pollution sources but also a considerable regional source over CEC. On the other hand, other types of OBB emissions had a certain impact on local  $PM_{2.5}$  concentrations in Jiangxi ( $9.04\%$ ), Fujian ( $11.82\%$ ), and Zhejiang ( $10.08\%$ ) but few effects ( $< 5\%$ ) on the other provinces.

### 3.6 Potential OCSB emission sources and associated meteorological causes

OCSB emissions can have significant impacts on local and regional haze in Henan, Anhui, Hubei, and Hunan. There is thus a need to explore associated potential sources and meteorological conditions. First, we utilized the CWT method to investigate potential OCSB emission sources triggering regional severe haze. To pinpoint potential emission sources for OCSB, Pingdingshan, Hefei, Wuhan, and Changsha were selected as receptor sites to represent Henan, Anhui, Hubei, and



Hunan, respectively. Figure 12 presents spatial distributions of the CWT values calculated based on the hybrid receptor  
490 model (Fig. S1) and observed  $\text{PM}_{2.5}$  concentrations for these cities. It should be noted that only sources with relatively high  
CWT values ( $> 150 \mu\text{g m}^{-3}$ ) were used as potential major sources leading to regional severe haze. For Henan and Anhui, most  
of the potential major sources concentrated in local areas with large amounts of OCSB emissions during EP2, thereby  
suggesting the dominant role of local OCSB emissions. For Hubei and Hunan, however, potential major sources were also  
located in common areas in Henan and Anhui, especially over the border between them, thus clearly demonstrating that local  
495 haze in Hubei and Hunan was caused by regional transport of pollution from Henan and Anhui. In summary, OCSB  
emissions in Henan and Anhui should be mainly responsible for regional haze over CEC during EP2.

Atmospheric pollution processes, especially wind fields, are closely related to synoptic weather patterns. A high-pressure  
system is usually considered to be the governing synoptic pattern suitable for the accumulation of air pollutants, whereas the  
differences between high and low-pressure systems are thought to be the major cause of transport on the regional scale.  
500 Figure 13 uses surface pressure maps from June 8 to 11 to explore the relationships among synoptic pressure patterns, OBB  
emissions, and haze formation over CEC. On June 8, concurrent with the OCSB outbreak, an extensive high-pressure system  
enveloped over CEC, forming a stationary condition and facilitating rapid accumulations of  $\text{PM}_{2.5}$  in Henan and Anhui.  
Thereafter, it was gradually turned into the low-pressure system on June 9 located at Jiangxi, receiving pollutants originating  
from Henan and Anhui by the differential field between the high- and low- pressure systems. This differential field also  
505 established positive dispersion conditions for Anhui, although OCSB emissions were still occurring there. Thereafter the  
stationary high-pressure system made a brief stay in Henan and Anhui on June 10, being prone to accumulate elevated  $\text{PM}_{2.5}$   
concentration, then a narrow low-pressure corridor squeezed by two high-pressure zones went through Henan, Hubei, and  
Hunan, thus facilitating regional transport of severe haze.

### 3.7 Comparison to previous studies

510 Numerous emission data on OBB have been established for CEC. These results, generally estimated based on statistics or  
satellite retrievals, have been rarely constrained by model and observations. Here we compare our constrained results with  
five representative emission datasets including GFASv1.0 (Kaiser et al., 2012), GFEDv4.1s (Van Der Werf et al., 2017),  
FINNv1.5 (Wiedinmyer et al., 2011), Qiu et al. (2016), and Zhou et al. (2017), as shown in Fig. 14. The former four  
inventories belong to satellite-based products, while the last one is derived with the traditional bottom-up method.  
515 Theoretically, there are two additional issues we need to note: (i) GFEDv4.1 incorporates small fires through the MODIS  
active fire detection product (Randerson et al., 2012); (ii) Qiu et al. (2016) is unable to discriminate small fires, but it can  
also detect more fire hotspots than GFASv1.0 and FINNv1.5 with the benefit of the extra MODIS burned area product  
(MCD64A1).

Figure 14 shows that the constrained OBB emissions in this study were generally higher than satellite-based estimates but  
520 lower than the bottom-up statistics (i.e., Zhou et al., 2017). For example, the constrained CO emissions over CEC were 5.2,  
3.4, and 5.7 times larger than those in GFASv1.0, GFEDv4.1s, and FINNv1.5, respectively. By comparison, the constrained



SO<sub>2</sub> and NO<sub>x</sub> emissions were also closer to those of GFED v4.1s. This indicates that small fires were projected to be central to OBB emissions since this OBB event was dominated by OCSB as mentioned, which always come from individual farmers with limited burned areas. In turn, for the NMVOCs, EC, OC, PM<sub>2.5</sub>, and PM<sub>10</sub>, our estimates were much higher than those from GFEDv4.1s but closer to those derived from Qiu et al. (2016) and Zhou et al. (2017) with the difference ranging from -10 % to 73 %. Thus, relative to substantial underestimations in GFEDv4.1s despite of additional small fires, such large increases in Qiu et al. (2016), which also acted as satellite-based estimates, should be attributed to extra detected fire hotspots. An emphasis should be given to Zhou et al. (2017), especially on higher SO<sub>2</sub>, CO, NO<sub>x</sub>, and NH<sub>3</sub> emissions (> 4 times), inevitably leading to unreasonable overestimations of PM<sub>2.5</sub> concentrations. On the other hand, it involves various uncertainties due to inherent statistical parameters and has common disadvantages in allocating seemingly sufficient emission amounts into high spatiotemporal cases.

In summary, the constrained OBB emissions in this study can not only supplement insufficient satellite-based estimates, but also to a large extent avoid overestimations due to inherently large uncertainties originating from bottom-up statistics.

In contrast to numerous OBB emission inventories for CEC, few studies focus on serious OBB events over CEC to investigate OBB contributions to surface PM<sub>2.5</sub>. Cheng et al. (2014) applied numerical models with satellite-based OBB emissions and found obvious OBB effects (i.e., 23 % ~ 48 %, 18 μg m<sup>-3</sup> ~ 65 μg m<sup>-3</sup>) on surface PM<sub>2.5</sub> in several cities over CEC (i.e., Ningbo, Shanghai, Nanjing, Hangzhou, and Suzhou) in June 2011. During the same period, Wu et al. (2017) utilized similar methods and found similar results in Nanjing (50 %). As expected, each of the two studies with raw satellite-based OBB emissions substantially underestimated surface PM<sub>2.5</sub> concentrations (-7 % ~ -38 %), especially in areas with intensive OBB activities at several times with peak concentrations (< -200 %). This would thus lead to relatively low estimates of OBB effects compared with our results. A most recent study (Yang and Zhao, 2019) adopted the constraining method, that is, similar to that in this study, to optimize OBB emissions for June 2012 but ignored the spatiotemporal heterogeneity of their adjustments, resulting in much more significant estimates of OBB effects (50 % ~ 70 %) than before, while slightly lower than those in our study. This implies that more detailed constrained methods, such as provinces-specific, even grids-specific adjustments, should be helpful to establish reliable OBB emissions with high spatial and temporal resolution over CEC.

#### 4 Conclusion and discussion

OBB, especially OCSB, has long been suspected of being the source of rapid deterioration of regional air quality over CEC during the harvest seasons. Up to now, satellite-based FINNv1.5 provides a unique opportunity to constrain variations in OBB and OCSB emissions with a high spatiotemporal resolution, despite substantial underestimations mainly resulting from unresolved agricultural small fires surrounding large fire hotspots. Here, we selected June 2014 as the study period, which includes a complete spatiotemporal evolution process (i.e., from June 1 to 19) of OBB and regional haze over CEC. We combined ground PM<sub>2.5</sub> measurements and model predictions with FINNv1.5 to constrain OBB emissions in terms of spatiotemporal variations. It is demonstrated that the constrained optimal emissions can allow the WRF-CMAQ to reproduce



555 spatiotemporal chemical fields induced by OBB more reasonably. By comparison, the optimal OBB emissions can, to a large  
extent, not only supplement insufficient estimations derived from satellite retrievals but also reduce overestimations of  
bottom-up methods. These model results were thus used to simultaneously isolate OBB and OCSB impacts on spatial and  
temporal evolutions of  $PM_{2.5}$  concentrations. Further, we employed the CWT method as well as analysis of surface pressure  
maps to explore potential major OBB sources and corresponding meteorological causes. These results can provide an  
560 effective and efficient reference for policymakers to improve environmental control strategies. The results are summarized as  
follows:

1. OCSB dominated OBB emissions during the study period by accounting for 74 ~ 94 %. And 81 ~ 88 % of OBB emissions  
intensively erupted during EP2 (from June 5 to 14). OBB mainly associated with OCSB emissions presented significant  
spatial and temporal inhomogeneities, mainly (> 60 %) concentrating in Henan and Anhui during EP2. Meanwhile, they had  
565 a strong spatiotemporal correlation with local haze in Henan and Anhui, indicating its critical role in affecting local  $PM_{2.5}$   
concentrations. In addition, they might also trigger regional haze in Hubei and Hunan through regional transport. By  
comparison, most of other types of OBB emission (> 71 %) were located in Anhui, Zhejiang, and Jiangxi.

2. The optimal adjustment coefficients for OBB emissions over CEC during the study period were not constant but varied  
depending on their spatial and temporal evolutions. Original FINNv1.5 roughly underestimated OBB emissions by a factor  
570 of 5 ~ 7 during EP2, but only a factor of 2 ~ 4 during EP1 and EP3. Specifically, with respect to Henan, Anhui, and other  
provinces over CEC, the optimal adjustment factors of OBB emissions were 6, 7, and 5 for EP2, respectively, whereas they  
were 4, 4, and 2 for EP1 and EP3, respectively.

3. With constrained optimal OBB emissions, the WRF-CMAQ model could reproduce chemical and meteorological fields  
reasonably during the study period from regional to provincial scales. Specifically, the model can capture the rapid outbreak  
575 of  $PM_{2.5}$  concentrations in Henan, Anhui, Hubei, and Henan. The correlation coefficients (R) between simulated and  
measured  $PM_{2.5}$  concentrations were higher than 0.6, and most of the corresponding NMB values were within 10 % over  
CEC.

4. OBB played a key role in reshaping spatial and temporal distributions of regional  $PM_{2.5}$  concentrations over CEC during  
the study period, and up to more than 89 % contributed by OCSB, especially in Henan, Anhui, Hubei, and Hunan during EP2.  
580 By comparison, other types of OBB also to a certain extent influenced the haze formation in Jiangxi, Fujian, and Zhejiang.

5. OCSB was not only a critical local pollution source but also had substantial impacts on the regional haze. Potential major  
OCSB emission sources leading to severe haze in Henan, Anhui, Hubei, and Hunan during EP2 were mostly located in  
Henan and Anhui, especially their borders. This finding highlights that effective and efficient OCSB controlling strategies  
were not implemented in these regions. Conversely, other types of OBBs only exhibited their impacts on local haze in Anhui,  
585 Zhejiang, and Jiangxi.

6. Stationary high-pressure systems led to relatively stable conditions in Henan and Anhui and thus played a cardinal role in  
enhancing local  $PM_{2.5}$  concentrations during EP2. Moreover, the conversions between the high- and low-pressure systems  
drive regional transport, directly facilitating the transports of accumulative pollutants from Henan and Anhui to Hubei,



Hunan, and Jiangxi. Therefore, interprovincial joint enforcement actions in terms of OBB prohibitions should be strictly undertaken.

It is a large challenge to detect small fires that are far from fire hotspots to reduce the uncertainties. Thus, one should take more satellite-based burning products in consideration. Besides, geostationary satellites might be the prospective means to overcome the limitation of time spans of polar-orbiting satellites. In addition, precise simulations of smoke plume and related chemical reactions are both challenging for regional and global models. The regional model is barely capable of characterizing turbulent flows of OBB plumes and subsequent vertical transport, thus causing uncertainties in three-dimensional distributions of aerosols viewed from a specific spatial and temporal scale. The constraining method combining model results and available observations could be an effective way to reduce large uncertainties in the OBB emission inventories. Furthermore, uniform optimal factors for all species of OBB emissions are used in this study. Thereby it is necessary to conduct species-specific adjustments in order to accurately investigate OBB effects. Similarly, provinces-specific, even grids-specific adjustments should also be further explored. Therefore, to improve the model capability in quantifying OBB and OCSB effects on regional air quality, more comprehensive experiments, field measurements and modelling efforts are needed in the future.

*Data availability.* MODIS and OMI data can be freely accessed at <https://earthdata.nasa.gov/> (last access: 5 August 2019). GFASv1.0 data are available from <http://apps.ecmwf.int/datasets/data/cams-gfas/> (last access: 5 August 2019). GFED4s data can be downloaded from [https://daac.ornl.gov/VEGETATION/guides/fire\\_emissions\\_v4.html](https://daac.ornl.gov/VEGETATION/guides/fire_emissions_v4.html) (last access: 5 August 2019). FINNv1.5 data can be found at <http://bai.acom.ucar.edu/Data/fire/> (last access: 5 August 2019).

*Supplement.* The supplement related to this article is available online.

*Author contributions.* SY and PL designed this study; SY, PL, KM, YW, LW, JS carried out analyses, interpreted data and wrote the manuscript. XC, ZL, YZ, ML, WL, YZ, DR contributed to the discussion. All authors have no competing interests.

*Competing interests.* The authors declare that they have no conflict of interest.

*Acknowledgements.* This study is supported by the Department of Science and Technology of China (No. 2016YFC0202702, 2018YFC0213506 and 2018YFC0213503), National Research Program for Key Issues in Air Pollution Control in China (No. DQGG0107) and National Natural Science Foundation of China (No. 21577126 and 41561144004). Pengfei Li is supported by Initiation Fund for Introducing Talents of Hebei Agricultural University (412201904).



## 620 References

- An, Z., Huang, R., Zhang, R., Tie, X., Li, G., Cao, J., Zhou, W., Shi, Z., Han, Y., Gu, Z. and others: Severe haze in Northern China: A synergy of anthropogenic emissions and atmospheric processes, *Proc. Natl. Acad. Sci.*, 116(18), 8657–8666, 2019.
- Andersson, A., Deng, J., Du, K., Zheng, M., Yan, C., Sköld, M. and Gustafsson, O.: Regionally-varying combustion sources of the January 2013 severe haze events over eastern China, *Environ. Sci. Technol.*, 49(4), 2038–2043, 2015.
- 625 Baró, R., Lorente-Plazas, R., Montávez, J. P. and Jiménez-Guerrero, P.: Biomass burning aerosol impact on surface winds during the 2010 Russian heat wave, *Geophys. Res. Lett.*, 44(2), 1088–1094, 2017.
- Bikkina, S., Andersson, A., Kirillova, E. N., Holmstrand, H., Tiwari, S., Srivastava, A. K., Bisht, D. S. and Gustafsson, Ö.: Air quality in megacity Delhi affected by countryside biomass burning, *Nat. Sustain.*, 1, 2019.
- Bond, T. C., Doherty, S. J., Fahey, D. W., Forster, P. M., Berntsen, T., DeAngelo, B. J., Flanner, M. G., Ghan, S., Kärcher, B., Koch, D. and others: Bounding the role of black carbon in the climate system: A scientific assessment, *J. Geophys. Res. Atmos.*, 118(11), 5380–5552, 2013.
- Byun, D. and Schere, K. L.: Review of the governing equations, computational algorithms, and other components of the Models-3 Community Multiscale Air Quality (CMAQ) modeling system, *Appl. Mech. Rev.*, 59(2), 51–77, 2006.
- Cao, G., Zhang, X., Wang, Y. and Zheng, F.: Estimation of emissions from field burning of crop straw in China, *Chinese Sci. Bull.*, 53(5), 784–790, 2008.
- 635 Carlton, A. G. and Baker, K. R.: Photochemical modeling of the Ozark isoprene volcano: MEGAN, BEIS, and their impacts on air quality predictions, *Environ. Sci. Technol.*, 45(10), 4438–4445, 2011.
- Carlton, A. G., Bhave, P. V., Napelenok, S. L., Edney, E. O., Sarwar, G., Pinder, R. W., Pouliot, G. A. and Houyoux, M.: Model representation of secondary organic aerosol in CMAQv4. 7, *Environ. Sci. Technol.*, 44(22), 8553–8560, 2010.
- 640 Chen, J., Li, C., Ristovski, Z., Milic, A., Gu, Y., Islam, M. S., Wang, S., Hao, J., Zhang, H., He, C. and others: A review of biomass burning: Emissions and impacts on air quality, health and climate in China, *Sci. Total Environ.*, 579, 1000–1034, 2017.
- Cheng, Y., Engling, G., He, K.-B., Duan, F.-K., Ma, Y.-L., Du, Z.-Y., Liu, J.-M., Zheng, M. and Weber, R. J.: Biomass burning contribution to Beijing aerosol, *Atmos. Chem. Phys.*, 13(15), 7765–7781, 2013.
- 645 Cheng, Z., Wang, S., Fu, X., Watson, J. G., Jiang, J., Fu, Q., Chen, C., Xu, B., Yu, J., Chow, J. C. and Hao, J.: Impact of biomass burning on haze pollution in the Yangtze River delta, China: a case study in summer 2011, *Atmos. Chem. Phys.*, 14(9), 4573–4585, doi:10.5194/acp-14-4573-2014, 2014.
- Choi, Y. and Fernando, H. J. S.: Implementation of a windblown dust parameterization into MODELS-3/CMAQ: Application to episodic PM events in the US/Mexico border, *Atmos. Environ.*, 42(24), 6039–6046, 2008.
- 650 Chuang, M., Fu, J., Lin, N., Lee, C., Gao, Y., Wang, S., Sheu, G., Hsiao, T., Wang, J., Yen, M. and others: Simulating the transport and chemical evolution of biomass burning pollutants originating from Southeast Asia during 7-SEAS/2010 Dongsha experiment, *Atmos. Environ.*, 112, 294–305, 2015.



- Clough, S. A., Shephard, M. W., Mlawer, E. J., Delamere, J. S., Iacono, M. J., Cady-Pereira, K., Boukabara, S. and Brown, P. D.: Atmospheric radiative transfer modeling: a summary of the AER codes, *J. Quant. Spectrosc. Radiat. Transf.*, 91(2), 233–244, 2005.
- Dai, Q., Bi, X., Song, W., Li, T., Liu, B., Ding, J., Xu, J., Song, C., Yang, N., Schulze, B. C. and others: Residential coal combustion as a source of primary sulfate in Xi'an, China, *Atmos. Environ.*, 196, 66–76, 2019.
- Digar, A. and Cohan, D. S.: Efficient characterization of pollutant-emission response under parametric uncertainty, *Environ. Sci. Technol.*, 44(17), 6724–6730, 2010.
- Fountoukis, C. and Nenes, A.: ISORROPIA II: a computationally efficient thermodynamic equilibrium model for  $K^+$ - $Ca^{2+}$ - $Mg^{2+}$ - $NH_4^+$ - $Na^+$ - $SO_4^{2-}$ - $NO_3^-$ - $Cl^-$ - $H_2O$  aerosols, *Atmos. Chem. Phys.*, 7(17), 4639–4659, 2007.
- Freitas, S. R., Longo, K. M. and Andreae, M. O.: Impact of including the plume rise of vegetation fires in numerical simulations of associated atmospheric pollutants, *Geophys. Res. Lett.*, 33(17), 2006.
- Fu, J. S., Hsu, N. C., Gao, Y., Huang, K., Li, C., Lin, N.-H. and Tsay, S.-C.: Evaluating the influences of biomass burning during 2006 BASE-ASIA: a regional chemical transport modeling, *Atmos. Chem. Phys.*, 12(9), 3837–3855, 2012a.
- Fu, P. Q., Kawamura, K., Chen, J., Li, J., Sun, Y. L., Liu, Y., Tachibana, E., Aggarwal, S. G., Okuzawa, K., Tanimoto, H. and others: Diurnal variations of organic molecular tracers and stable carbon isotopic composition in atmospheric aerosols over Mt. Tai in the North China Plain: an influence of biomass burning, *Atmos. Chem. Phys.*, 12(18), 8359–8375, 2012b.
- Gao, M., Carmichael, G. R., Wang, Y., Saide, P. E., Yu, M., Xin, J., Liu, Z. and Wang, Z.: Modeling study of the 2010 regional haze event in the North China Plain, *Atmos. Chem. Phys.*, 16(3), 1673, 2016.
- Hamilton, D. S., Hantson, S., Scott, C. E., Kaplan, J. O., Pringle, K. J., Nieradzik, L. P., Rap, A., Folberth, G. A., Spracklen, D. V and Carslaw, K. S.: Reassessment of pre-industrial fire emissions strongly affects anthropogenic aerosol forcing, *Nat. Commun.*, 9(1), 3182, 2018.
- Hong, J., Ren, L., Hong, J. and Xu, C.: Environmental impact assessment of corn straw utilization in China, *J. Clean. Prod.*, 112, 1700–1708, 2016.
- Hooghiemstra, P. B., Krol, M. C., Van Leeuwen, T. T., Van Der Werf, G. R., Novelli, P. C., Deeter, M. N., Aben, I. and Röckmann, T.: Interannual variability of carbon monoxide emission estimates over South America from 2006 to 2010, *J. Geophys. Res. Atmos.*, 117(D15), 2012.
- Hsu, Y., Holsen, T. M. and Hopke, P. K.: Comparison of hybrid receptor models to locate PCB sources in Chicago, *Atmos. Environ.*, 37(4), 545–562, 2003.
- Hu, J., Wu, L., Zheng, B., Zhang, Q., He, K., Chang, Q., Li, X., Yang, F., Ying, Q. and Zhang, H.: Source contributions and regional transport of primary particulate matter in China, *Environ. Pollut.*, 207, 31–42, 2015.
- Huang, R.-J., Zhang, Y., Bozzetti, C., Ho, K.-F., Cao, J.-J., Han, Y., Daellenbach, K. R., Slowik, J. G., Platt, S. M., Canonaco, F. and others: High secondary aerosol contribution to particulate pollution during haze events in China, *Nature*, 514(7521), 218, 2014.



- Huang, X., Ding, A., Liu, L., Liu, Q., Ding, K., Niu, X., Nie, W., Xu, Z., Chi, X., Wang, M. and others: Effects of aerosol-radiation interaction on precipitation during biomass-burning season in East China., *Atmos. Chem. Phys.*, 16(15), 2016.
- Hyer, E. J., Allen, D. J. and Kasischke, E. S.: Examining injection properties of boreal forest fires using surface and satellite measurements of CO transport, *J. Geophys. Res. Atmos.*, 112(D18), 2007.
- 690 Janssens-Maenhout, G., Crippa, M., Guizzardi, D., Dentener, F., Muntean, M., Pouliot, G., Keating, T., Zhang, Q., Kurokawa, J., Wankmüller, R. and others: HTAP\_v2. 2: a mosaic of regional and global emission grid maps for 2008 and 2010 to study hemispheric transport of air pollution, *Atmos. Chem. Phys.*, 15(19), 11411–11432, 2015.
- Kain, J. S.: The Kain-Fritsch convective parameterization: an update, *J. Appl. Meteorol.*, 43(1), 170–181, 2004.
- Kaiser, J. W., Heil, A., Andreae, M. O., Benedetti, A., Chubarova, N., Jones, L., Morcrette, J. J., Razinger, M., Schultz, M.
- 695 G., Suttie, M. and others: Biomass burning emissions estimated with a global fire assimilation system based on observed fire radiative power, 2012.
- Konovalov, I. B., Berezin, E. V., Ciais, P., Broquet, G., Beekmann, M., Hadji-Lazaro, J., Clerbaux, C., Andreae, M. O., Kaiser, J. W. and Schulze, E. D.: Constraining CO<sub>2</sub> emissions from open biomass burning by satellite observations of co-emitted species: a method and its application to wildfires in Siberia, *Atmos. Chem. Phys.*, 14, 10383–10410, 2014.
- 700 Laing, J. R., Jaffe, D. A. and Hee, J. R.: Physical and optical properties of aged biomass burning aerosol from wildfires in Siberia and the Western USA at the Mt. Bachelor Observatory, *Atmos. Chem. Phys.*, 16(23), 15185–15197, 2016.
- Lee, H., Iraqi, O., Gu, Y., Yim, S. H., Chulakadabba, A., Tonks, A. Y.-M., Yang, Z. and Wang, C.: Impacts of air pollutants from fire and non-fire emissions on the regional air quality in Southeast Asia, *Atmos. Chem. Phys.*, 18(9), 6141–6156, 2018.
- 705 Lei, W., Li, G. and Molina, L. T.: Modeling the impacts of biomass burning on air quality in and around Mexico City, *Atmos. Chem. Phys.*, 13(5), 2299–2319, 2013.
- Leung, F., Logan, J. A., Park, R., Hyer, E., Kasischke, E., Streets, D. and Yurganov, L.: Impacts of enhanced biomass burning in the boreal forests in 1998 on tropospheric chemistry and the sensitivity of model results to the injection height of emissions, *J. Geophys. Res. Atmos.*, 112(D10), 2007.
- 710 Li, H., Zhang, Q., Zhang, Q., Chen, C., Wang, L., Wei, Z., Zhou, S., Parworth, C., Zheng, B., Canonaco, F. and others: Wintertime aerosol chemistry and haze evolution in an extremely polluted city of the North China Plain: significant contribution from coal and biomass combustion, *Atmos. Chem. Phys.*, 17(7), 4751–4768, 2017a.
- Li, J., Li, Y., Bo, Y. and Xie, S.: High-resolution historical emission inventories of crop residue burning in fields in China for the period 1990–2013, *Atmos. Environ.*, 138, 152–161, 2016.
- 715 Li, M., Zhang, Q., Kurokawa, J.-I., Woo, J. H., He, K. B., Lu, Z., Ohara, T., Song, Y., Streets, D. G., Carmichael, G. R. and others: MIX: a mosaic Asian anthropogenic emission inventory for the MICS-Asia and the HTAP projects, *Atmos. Chem. Phys. Discuss.*, 15(23), 34813–34869, 2015a.



- Li, M., Zhang, Q., Kurokawa, J., Woo, J.-H., He, K., Lu, Z., Ohara, T., Song, Y., Streets, D. G., Carmichael, G. R. and others: MIX: a mosaic Asian anthropogenic emission inventory under the international collaboration framework of the  
720 MICS-Asia and HTAP, *Atmos. Chem. Phys.*, 17(2), 2017b.
- Li, P., Yan, R., Yu, S., Wang, S., Liu, W. and Bao, H.: Reinstate regional transport of PM<sub>2.5</sub> as a major cause of severe haze in Beijing, *Proc. Natl. Acad. Sci.*, 112(21), E2739--E2740, 2015b.
- Li, W., Shao, L. and Buseck, P. R.: Haze types in Beijing and the influence of agricultural biomass burning, *Atmos. Chem. Phys.*, 10(17), 8119–8130, doi:10.5194/acp-10-8119-2010, 2010.
- 725 Li, X., Wang, S., Duan, L., Hao, J., Li, C., Chen, Y. and Yang, L.: Particulate and trace gas emissions from open burning of wheat straw and corn stover in China, *Environ. Sci. Technol.*, 41(17), 6052–6058, 2007.
- Li, X., Han, J., Hopke, P. K., Hu, J., Shu, Q., Chang, Q. and Ying, Q.: Quantifying primary and secondary humic-like substances in urban aerosol based on emission source characterization and a source-oriented air quality model, *Atmos. Chem. Phys.*, 19(4), 2327–2341, 2019.
- 730 Li, Z., Guo, J., Ding, A., Liao, H., Liu, J., Sun, Y., Wang, T., Xue, H., Zhang, H. and Zhu, B.: Aerosol and boundary-layer interactions and impact on air quality, *Natl. Sci. Rev.*, 4(6), 810–833, 2017c.
- Liu, H., Wu, B., Liu, S., Shao, P., Liu, X., Zhu, C., Wang, Y., Wu, Y., Xue, Y., Gao, J. and others: A regional high-resolution emission inventory of primary air pollutants in 2012 for Beijing and the surrounding five provinces of North China, *Atmos. Environ.*, 181, 20–33, 2018a.
- 735 Liu, J., Mauzerall, D. L., Chen, Q., Zhang, Q., Song, Y., Peng, W., Klimont, Z., Qiu, X., Zhang, S., Hu, M. and others: Air pollutant emissions from Chinese households: A major and underappreciated ambient pollution source, *Proc. Natl. Acad. Sci.*, 113(28), 7756–7761, 2016.
- Liu, M., Song, Y., Yao, H., Kang, Y., Li, M., Huang, X. and Hu, M.: Estimating emissions from agricultural fires in the North China Plain based on MODIS fire radiative power, *Atmos. Environ.*, 112, 326–334, 2015.
- 740 Liu, M., Lin, J., Wang, Y., Sun, Y., Zheng, B., Shao, J., Chen, L., Zheng, Y., Chen, J., Fu, T.-M. and others: Spatiotemporal variability of NO<sub>2</sub> and PM<sub>2.5</sub> over Eastern China: observational and model analyses with a novel statistical method, *Atmos. Chem. Phys.*, 18(17), 12933–12952, 2018b.
- Liu, S., Hua, S., Wang, K., Qiu, P., Liu, H., Wu, B., Shao, P., Liu, X., Wu, Y., Xue, Y. and others: Spatial-temporal variation characteristics of air pollution in Henan of China: Localized emission inventory, WRF/Chem simulations and potential  
745 source contribution analysis, *Sci. Total Environ.*, 624, 396–406, 2018c.
- Liu, X., Zhang, Y., Cheng, S., Xing, J., Zhang, Q., Streets, D. G., Jang, C., Wang, W. and Hao, J.: Understanding of regional air pollution over China using CMAQ, part I performance evaluation and seasonal variation, *Atmos. Environ.*, 44(20), 2415–2426, 2010.
- Lo, J., Yang, Z. and Pielke Sr, R. A.: Assessment of three dynamical climate downscaling methods using the Weather  
750 Research and Forecasting (WRF) model, *J. Geophys. Res. Atmos.*, 113(D9), 2008.



- Long, X., Tie, X., Cao, J., Huang, R., Feng, T., Li, N., Zhao, S., Tian, J., Li, G. and Zhang, Q.: Impact of crop field burning and mountains on heavy haze in the North China Plain: a case study., *Atmos. Chem. Phys.*, 16(15), 2016.
- Malavelle, F. F., Haywood, J. M., Mercado, L. M., Folberth, G. A., Bellouin, N., Sitch, S. and Artaxo, P.: Studying the impact of biomass burning aerosol radiative and climate effects on the Amazon rainforest productivity with an Earth system model, *Atmos. Chem. Phys.*, 19(2), 1301–1326, 2019.
- 755 Mehmood, K., Chang, S., Yu, S., Wang, L., Li, P., Li, Z., Liu, W., Rosenfeld, D. and Seinfeld, J. H.: Spatial and temporal distributions of air pollutant emissions from open crop straw and biomass burnings in China from 2002 to 2016, *Environ. Chem. Lett.*, 16(1), 301–309, 2018.
- Monks, S. A., Arnold, S. R., Emmons, L. K., Law, K. S., Turquety, S., Duncan, B. N., Flemming, J., Huijnen, V., Tilmes, S., Langner, J. and others: Multi-model study of chemical and physical controls on transport of anthropogenic and biomass burning pollution to the Arctic, *Atmos. Chem. Phys.*, 15(6), 3575–3603, 2015.
- 760 Morrison, H. and Gettelman, A.: A new two-moment bulk stratiform cloud microphysics scheme in the Community Atmosphere Model, version 3 (CAM3). Part I: Description and numerical tests, *J. Clim.*, 21(15), 3642–3659, 2008.
- Pimonsree, S., Vongruang, P. and Sumitsawan, S.: Modified biomass burning emission in modeling system with fire radiative power: Simulation of particulate matter in Mainland Southeast Asia during smog episode, *Atmos. Pollut. Res.*, 9(1), 133–145, 2018.
- 765 Pleim, J. E.: A combined local and nonlocal closure model for the atmospheric boundary layer. Part I: Model description and testing, *J. Appl. Meteorol. Climatol.*, 46(9), 1383–1395, 2007a.
- Pleim, J. E.: A combined local and nonlocal closure model for the atmospheric boundary layer. Part II: Application and evaluation in a mesoscale meteorological model, *J. Appl. Meteorol. Climatol.*, 46(9), 1396–1409, 2007b.
- 770 Qiao, X., Guo, H., Tang, Y., Wang, P., Deng, W., Zhao, X., Hu, J., Ying, Q. and Zhang, H.: Local and regional contributions to fine particulate matter in the 18 cities of Sichuan Basin, southwestern China, *Atmos. Chem. Phys.*, 19(9), 5791–5803, 2019.
- Qin, Y. and Xie, S. D.: Historical estimation of carbonaceous aerosol emissions from biomass open burning in China for the period 1990–2005, *Environ. Pollut.*, 159(12), 3316–3323, 2011.
- 775 Qiu, X., Duan, L., Chai, F., Wang, S., Yu, Q. and Wang, S.: Deriving high-resolution emission inventory of open biomass burning in China based on satellite observations, *Environ. Sci. Technol.*, 50(21), 11779–11786, 2016.
- Randerson, J. T., Chen, Y., Van Der Werf, G. R., Rogers, B. M. and Morton, D. C.: Global burned area and biomass burning emissions from small fires, *J. Geophys. Res. Biogeosciences*, 117(G4), 2012.
- 780 Saleh, R., Robinson, E. S., Tkacik, D. S., Ahern, A. T., Liu, S., Aiken, A. C., Sullivan, R. C., Presto, A. A., Dubey, M. K., Yokelson, R. J. and others: Brownness of organics in aerosols from biomass burning linked to their black carbon content, *Nat. Geosci.*, 7(9), 647, 2014.
- Seinfeld, J. H. and Pandis, S. N.: *Atmospheric chemistry and physics: from air pollution to climate change*, John Wiley & Sons., 2016.



- 785 Singh, N., Banerjee, T., Raju, M. P., Deboudt, K., Sorek-Hamer, M., Singh, R. S. and Mall, R. K.: Aerosol chemistry, transport, and climatic implications during extreme biomass burning emissions over the Indo-Gangetic Plain., *Atmos. Chem. Phys.*, 18(19), 2018.
- Stein, A. F., Draxler, R. R., Rolph, G. D., Stunder, B. J. B., Cohen, M. D. and Ngan, F.: NOAA's HYSPLIT atmospheric transport and dispersion modeling system, *Bull. Am. Meteorol. Soc.*, 96(12), 2059–2077, 2015.
- 790 Streets, D. G., Yarber, K. F., Woo, J.-H. and Carmichael, G. R.: Biomass burning in Asia: Annual and seasonal estimates and atmospheric emissions, *Global Biogeochem. Cycles*, 17(4), 2003.
- Sun, Y., Jiang, Q., Xu, Y., Ma, Y., Zhang, Y., Liu, X., Li, W., Wang, F., Li, J., Wang, P. and others: Aerosol characterization over the North China Plain: Haze life cycle and biomass burning impacts in summer, *J. Geophys. Res. Atmos.*, 121(5), 2508–2521, 2016.
- 795 Tai, E., Jimenez, M., Nopmongkol, O., Wilson, G., Mansell, G., Koo, B. and Yarwood, G.: Boundary conditions and fire emissions modeling, *Prep. Texas Comm. Environ. Qual.* Sept., 2008.
- Tang, X., Zhu, J., Wang, Z. F. and Gbaguidi, A.: Improvement of ozone forecast over Beijing based on ensemble Kalman filter with simultaneous adjustment of initial conditions and emissions, *Atmos. Chem. Phys.*, 11(24), 12901–12916, 2011.
- Tsao, C. C., Campbell, J. E., Mena-Carrasco, M., Spak, S. N., Carmichael, G. R. and Chen, Y.: Increased estimates of air-pollution emissions from Brazilian sugar-cane ethanol, *Nat. Clim. Chang.*, 2(1), 53, 2012.
- 800 Uranishi, K., Ikemori, F., Shimadera, H., Kondo, A. and Sugata, S.: Impact of field biomass burning on local pollution and long-range transport of PM<sub>2.5</sub> in Northeast Asia, *Environ. Pollut.*, 244, 414–422, 2019.
- Vakkari, V., Beukes, J. P., Dal Maso, M., Aurela, M., Josipovic, M. and van Zyl, P. G.: Major secondary aerosol formation in southern African open biomass burning plumes, *Nat. Geosci.*, 11(8), 580, 2018.
- 805 Wang, J., Wang, S., Jiang, J., Ding, A., Zheng, M., Zhao, B., Wong, D. C., Zhou, W., Zheng, G., Wang, L. and others: Impact of aerosol–meteorology interactions on fine particle pollution during China's severe haze episode in January 2013, *Environ. Res. Lett.*, 9(9), 94002, 2014.
- Wang, L., Xu, J., Yang, J., Zhao, X., Wei, W., Cheng, D., Pan, X. and Su, J.: Understanding haze pollution over the southern Hebei area of China using the CMAQ model, *Atmos. Environ.*, 56, 69–79, 2012.
- 810 Wang, M., Cao, C., Li, G. and Singh, R. P.: Analysis of a severe prolonged regional haze episode in the Yangtze River Delta, China, *Atmos. Environ.*, 102, 112–121, 2015.
- Wang, P., Ying, Q., Zhang, H., Hu, J., Lin, Y. and Mao, H.: Source apportionment of secondary organic aerosol in China using a regional source-oriented chemical transport model and two emission inventories, *Environ. Pollut.*, 237, 756–766, 2018.
- 815 Wang, Y., Zhang, X., Draxler, R. R. and others: TrajStat: GIS-based software that uses various trajectory statistical analysis methods to identify potential sources from long-term air pollution measurement data, *Environ. Model. Softw.*, 24(8), 938–939, 2009.



- Washenfeller, R. A., Attwood, A. R., Brock, C. A., Guo, H., Xu, L., Weber, R. J., Ng, N. L., Allen, H. M., Ayres, B. R.,  
Baumann, K. and others: Biomass burning dominates brown carbon absorption in the rural southeastern United States,  
820 *Geophys. Res. Lett.*, 42(2), 653–664, 2015.
- Van Der Werf, G. R., Randerson, J. T., Giglio, L., Van Leeuwen, T. T., Chen, Y., Rogers, B. M., Mu, M., Van Marle, M. J.  
E., Morton, D. C., Collatz, G. J. and others: Global fire emissions estimates during 1997–2016, 2017.
- Wiedinmyer, C., Akagi, S. K., Yokelson, R. J., Emmons, L. K., Al-Saadi, J. A., Orlando, J. J. and Soja, A. J.: The Fire  
INventory from NCAR (FINN): a high resolution global model to estimate the emissions from open burning, *Geosci. Model*  
825 *Dev.*, 4(3), 625, 2011.
- Wong, D. C., Pleim, J., Mathur, R., Binkowski, F., Otte, T., Gilliam, R., Pouliot, G., Xiu, A., Young, J. O. and Kang, D.:  
WRF-CMAQ two-way coupled system with aerosol feedback: software development and preliminary results, *Geosci. Model*  
*Dev.*, 5(2), 299–312, 2012.
- Wu, J., Kong, S., Wu, F., Cheng, Y., Zheng, S., Yan, Q., Zheng, H., Yang, G., Zheng, M., Liu, D. and others: Estimating the  
830 open biomass burning emissions in central and eastern China from 2003 to 2015 based on satellite observation., *Atmos.*  
*Chem. Phys.*, 18(16), 2018.
- Wu, Y., Han, Y., Voulgarakis, A., Wang, T., Li, M., Wang, Y., Xie, M., Zhuang, B. and Li, S.: An agricultural biomass  
burning episode in eastern China: Transport, optical properties, and impacts on regional air quality, *J. Geophys. Res. Atmos.*,  
122(4), 2304–2324, 2017.
- 835 Xiao, X., Cohan, D. S., Byun, D. W. and Ngan, F.: Highly nonlinear ozone formation in the Houston region and implications  
for emission controls, *J. Geophys. Res. Atmos.*, 115(D23), 2010.
- Xiu, A. and Pleim, J. E.: Development of a land surface model. Part I: Application in a mesoscale meteorological model, *J.*  
*Appl. Meteorol.*, 40(2), 192–209, 2001.
- Xu, Y., Huang, Z., Jia, G., Fan, M., Cheng, L., Chen, L., Shao, M. and Zheng, J.: Regional discrepancies in spatiotemporal  
840 variations and driving forces of open crop residue burning emissions in China, *Sci. Total Environ.*, 2019.
- Yamaji, K., Li, J., Uno, I., Kanaya, Y., Irie, H., Takigawa, M., Komazaki, Y., Pochanart, P., Liu, Y., Tanimoto, H. and  
others: Impact of open crop residual burning on air quality over Central Eastern China during the Mount Tai Experiment  
2006 (MTX2006), *Atmos. Chem. Phys.*, 10(15), 7353–7368, 2010.
- Yan, X., Ohara, T. and Akimoto, H.: Bottom-up estimate of biomass burning in mainland China, *Atmos. Environ.*, 40(27),  
845 5262–5273, 2006.
- Yang, Y. and Zhao, Y.: Quantification and evaluation of atmospheric pollutant emissions from open biomass burning with  
multiple methods: a case study for the Yangtze River Delta region, China, *Atmos. Chem. Phys.*, 19(1), 327–348, 2019.
- Yarwood, G., Rao, S., Yocke, M. and Whitten, G. Z.: Updates to the carbon bond chemical mechanism: CB05, Final Rep. to  
US EPA, RT-0400675, 8, 2005.
- 850 Yu, M., Yuan, X., He, Q., Yu, Y., Cao, K., Yang, Y. and Zhang, W.: Temporal-spatial analysis of crop residue burning in  
China and its impact on aerosol pollution, *Environ. Pollut.*, 245, 616–626, 2019.



- Yu, S., Eder, B., Dennis, R., Chu, S.-H. and Schwartz, S. E.: New unbiased symmetric metrics for evaluation of air quality models, *Atmos. Sci. Lett.*, 7(1), 26–34, 2006.
- 855 Yu, S., Mathur, R., Pleim, J., Pouliot, G., Wong, D., Eder, B., Schere, K., Gilliam, R. and Rao, S. T.: Comparative evaluation of the impact of WRF/NMM and WRF/ARW meteorology on CMAQ simulations for PM 2.5 and its related precursors during the 2006 TexAQS/GoMACCS study, *Atmos. Chem. Phys.*, 12(9), 4091–4106, 2012.
- Yu, S., Mathur, R., Pleim, J., Wong, D., Gilliam, R., Alapaty, K., Zhao, C. and Liu, X.: Aerosol indirect effect on the grid-scale clouds in the two-way coupled WRF-CMAQ: model description, development, evaluation and regional analysis, *Atmos. Chem. Phys. Discuss.*, 25649, 2013.
- 860 Yu, S., Zhang, Q., Yan, R., Wang, S., Li, P., Chen, B., Liu, W. and Zhang, X.: Origin of air pollution during a weekly heavy haze episode in Hangzhou, China, *Environ. Chem. Lett.*, 12(4), 543–550, 2014.
- Yu, S., Li, P., Wang, L., Wu, Y., Wang, S., Liu, K., Zhu, T., Zhang, Y., Hu, M., Zeng, L. and others: Mitigation of severe urban haze pollution by a precision air pollution control approach, *Sci. Rep.*, 8(1), 8151, 2018.
- Yuyun, B., Yajing, W. and Chunyu, G.: Straw Resource Quantity and its Regional Distribution in China [J], *J. Agric. Mech. Res.*, 3(3), 1–7, 2010.
- 865 Zhang, H., Hu, J., Qi, Y., Li, C., Chen, J., Wang, X., He, J., Wang, S., Hao, J., Zhang, L. and others: Emission characterization, environmental impact, and control measure of PM<sub>2.5</sub> emitted from agricultural crop residue burning in China, *J. Clean. Prod.*, 149, 629–635, 2017.
- Zhang, L., Liu, Y. and Hao, L.: Contributions of open crop straw burning emissions to PM<sub>2.5</sub> concentrations in China, *Environ. Res. Lett.*, 11(1), 14014, 2016a.
- 870 Zhang, T., Wooster, M. J., Green, D. C. and Main, B.: New field-based agricultural biomass burning trace gas, PM<sub>2.5</sub>, and black carbon emission ratios and factors measured in situ at crop residue fires in Eastern China, *Atmos. Environ.*, 121, 22–34, 2015a.
- Zhang, X., Lu, Y., Wang, Q. and Qian, X.: A high-resolution inventory of air pollutant emissions from crop residue burning in China, *Atmos. Environ.*, 2019.
- 875 Zhang, X. Y., Wang, J. Z., Wang, Y. Q., Liu, H. L., Sun, J. Y. and Zhang, Y. M.: Changes in chemical components of aerosol particles in different haze regions in China from 2006 to 2013 and contribution of meteorological factors, *Atmos. Chem. Phys.*, 15(22), 12935–12952, 2015b.
- Zhang, Y.-L. and Cao, F.: Is it time to tackle PM<sub>2.5</sub> air pollutions in China from biomass-burning emissions?, *Environ. Pollut.*, 202, 217–219, 2015.
- 880 Zhang, Y., Shao, M., Lin, Y., Luan, S., Mao, N., Chen, W. and Wang, M.: Emission inventory of carbonaceous pollutants from biomass burning in the Pearl River Delta Region, China, *Atmos. Environ.*, 76, 189–199, 2013.
- Zhang, Y., Zhang, X., Wang, K., Zhang, Q., Duan, F. and He, K.: Application of WRF/Chem over East Asia: Part II. Model improvement and sensitivity simulations, *Atmos. Environ.*, 124, 301–320, 2016b.



- 885 Zhao, C., Liu, X., Leung, L. R., Johnson, B., McFarlane, S. A., Gustafson Jr, W. I., Fast, J. D. and Easter, R.: The spatial distribution of mineral dust and its shortwave radiative forcing over North Africa: modeling sensitivities to dust emissions and aerosol size treatments, *Atmos. Chem. Phys.*, 10(18), 8821–8838, 2010.
- Zhao, Y., Mao, P., Zhou, Y., Yang, Y., Zhang, J., Wang, S., Dong, Y., Xie, F., Yu, Y. and Li, W.: Improved provincial emission inventory and speciation profiles of anthropogenic non-methane volatile organic compounds: a case study for Jiangsu, China, *Atmos. Chem. Phys.*, 17(12), 7733–7756, 2017.
- 890 Zhou, Y., Xing, X., Lang, J., Chen, D., Cheng, S., Lin, W., Xiao, W. and Liu, C.: A comprehensive biomass burning emission inventory with high spatial and temporal resolution in China, *Atmos. Chem. Phys.*, 17(4), 2839, 2017.
- Zhou, Y., Han, Z., Liu, R., Zhu, B., Li, J. and Zhang, R.: A modeling study of the impact of crop residue burning on PM<sub>2.5</sub> concentration in Beijing and Tianjin during a severe autumn haze event, *Aerosol Air Qual. Res.*, 18(7), 1558–1572, 2018.
- 895 Zhuang, Y., Li, R., Yang, H., Chen, D., Chen, Z., Gao, B. and He, B.: Understanding temporal and spatial distribution of crop residue burning in China from 2003 to 2017 Using MODIS Data, *Remote Sens.*, 10(3), 390, 2018.

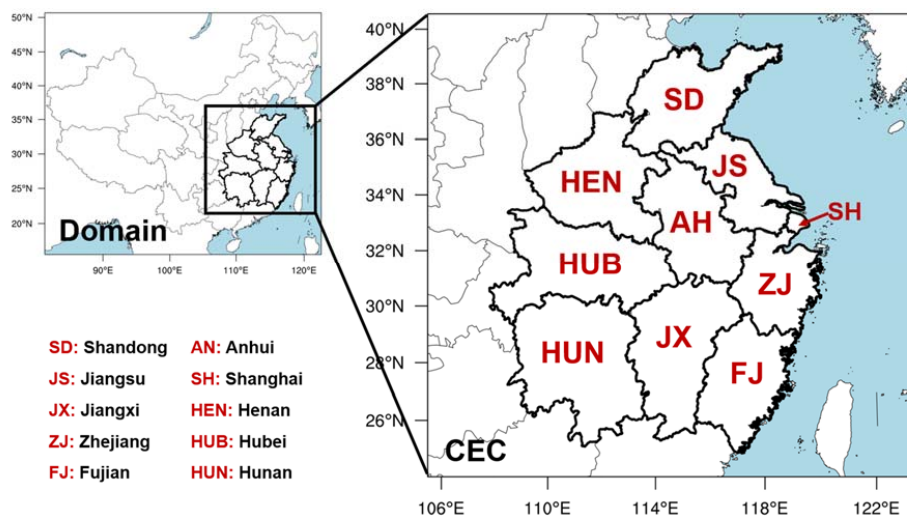


Figure 1. Model domain and geographical areas of CEC. Black thick lines outline boundaries of 10 provinces belonging to CEC, including Anhui (AH), Hubei (HB), Henan (HEN), Hunan (HUN), Shandong (SD), Zhejiang (ZJ), Jiangsu (JS), Shanghai (SH), Fujian (FJ) and Jiangxi (JX). This figure is generated using NCAR Command Language (NCL) version 6.3.0, open-source software

5 free to the public.

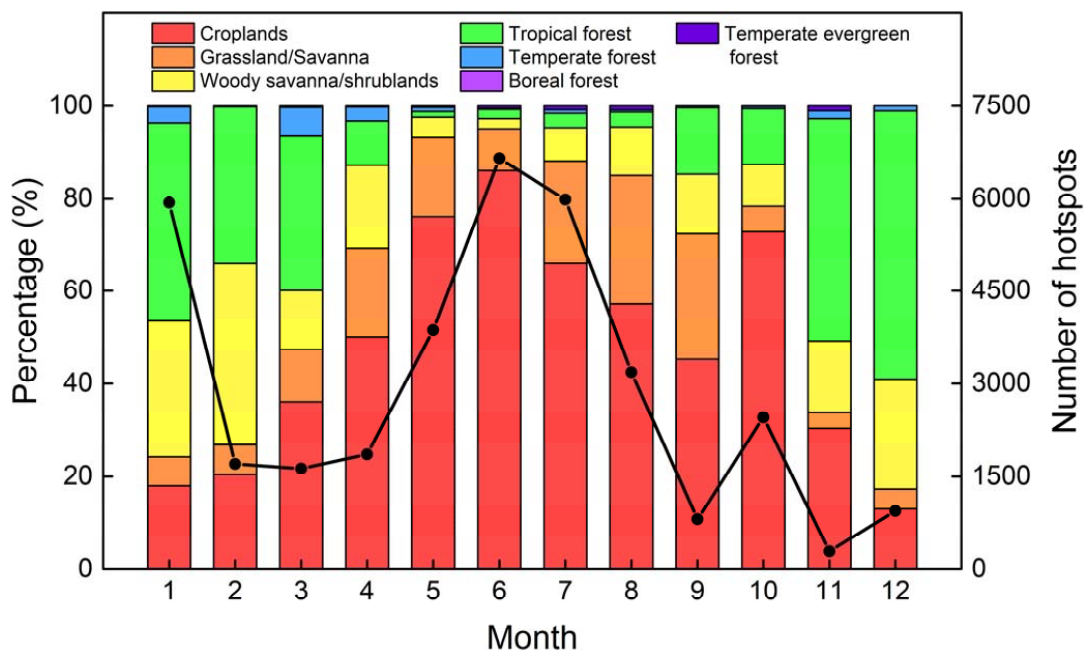
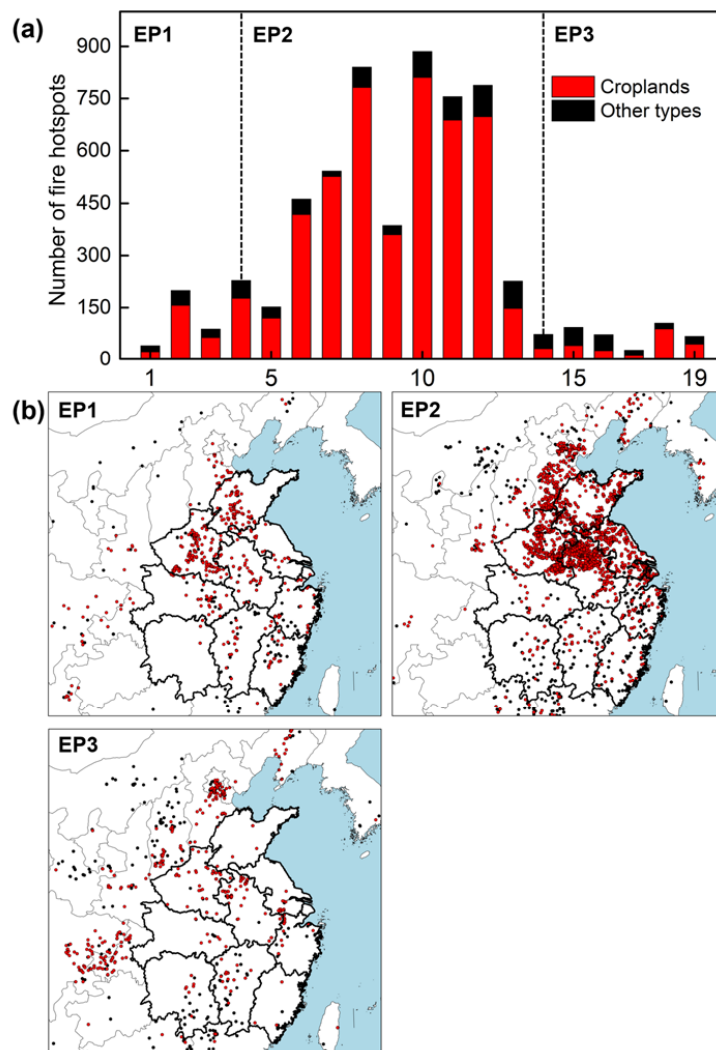
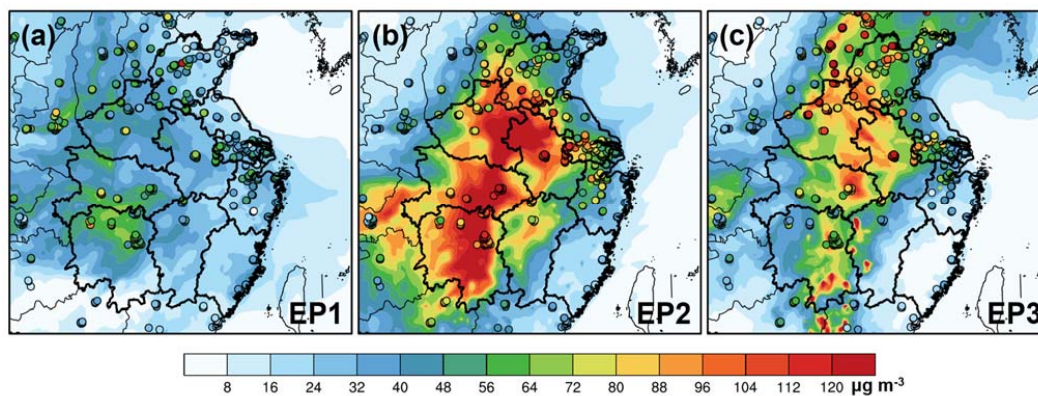


Figure 2. Monthly variations in numbers of OBB fire hotspots in FINNv1.5 over CEC (right axis) in 2014 and relative contributions of seven types of OBB classified by corresponding land use types (left axis).

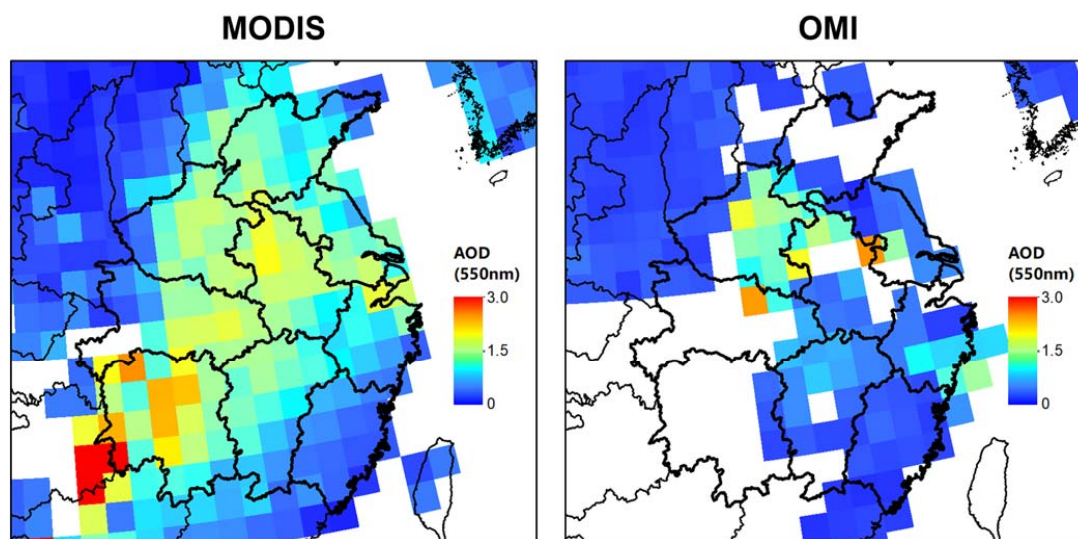


10

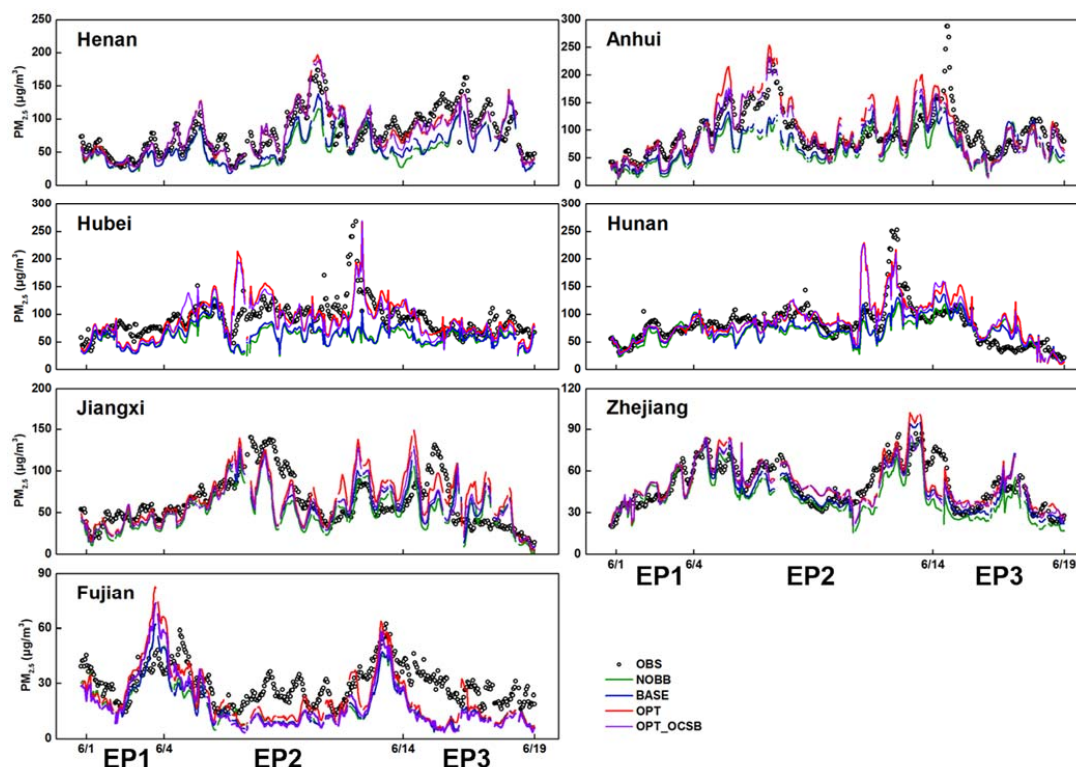
Figure 3. (a) Temporal and (b) spatial variations in numbers of fire hotspots for OCSB and other types of OBB during EP1, EP2 and EP3, which represent three successive episodes in turn, namely, from June 1 to 4, June 5 to 14, and June 15 to 19, respectively. This figure is generated using NCAR Command Language (NCL) version 6.3.0, open-source software free to the public.



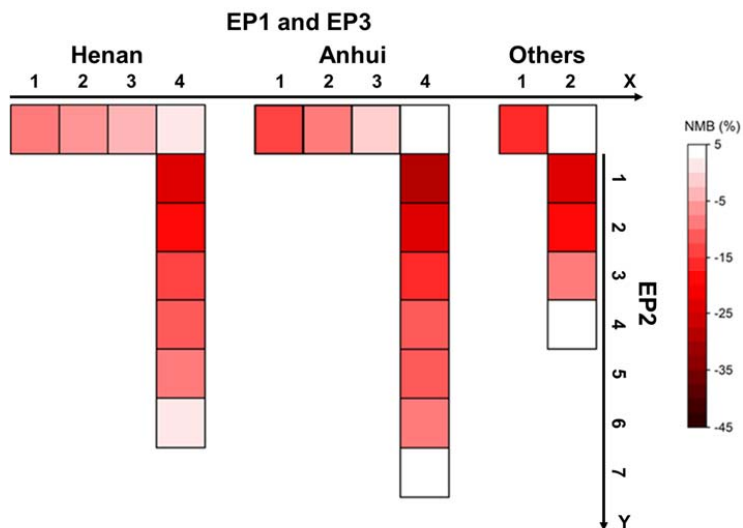
15 Figure 4. Spatial distributions of simulated and observed episode-averaged PM<sub>2.5</sub> concentrations over CEC during (a) EP1, (b) EP2, and (c) EP3. Colored circles denotes locations of ground measurement sites and corresponding values. This figure is generated using NCAR Command Language (NCL) version 6.3.0, open-source software free to the public.



20 Figure 5. Spatial distributions of AOD observed by MODIS (MOD08\_D3) at 550 nm and OMI (OMERUVd v003) at 500 nm for EP2. This figure is generated using NCAR Command Language (NCL) version 6.3.0, open-source software free to the public.



25 **Figure 6.** Provincial average temporal variations in ground observed and simulated hourly  $PM_{2.5}$  concentrations in Henan, Anhui, Hubei, Hunan, Jiangxi, Zhejiang and Fujian. The averaged concentrations for each province were calculated with values at the monitoring stations from both observations and different model simulations (OBS: observations; NOBB: the simulations with only anthropogenic and biogenic emissions; BASE: the simulations with not only anthropogenic and biogenic emissions but also original OBB emissions in FINNv1.5; OPT: the simulations with not only anthropogenic and biogenic emissions but also constrained OBB emissions; OPT\_OCSB: the simulations with not only anthropogenic and biogenic emissions but also constrained OCSB emissions)



30

Figure 7. Model responses to dynamic emission perturbations. Colored cells represent NMBs between observed and simulated  $PM_{2.5}$  concentrations in different model sensitive tests for Henan, Anhui and other provinces over CEC. Coefficients in X axis refer to the adjustment coefficients for OBB emissions in EP1 and EP3, while coefficients in Y axis denotes the ones for EP2.

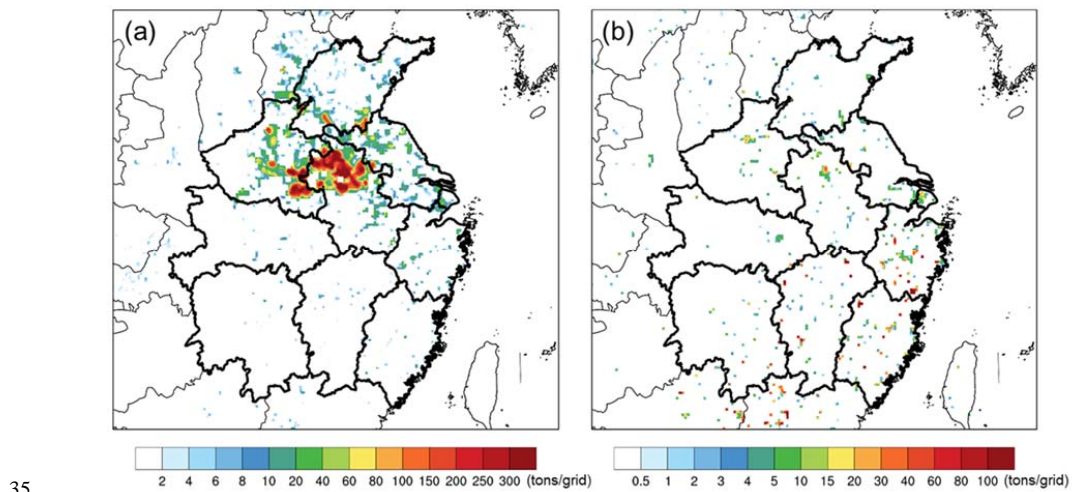
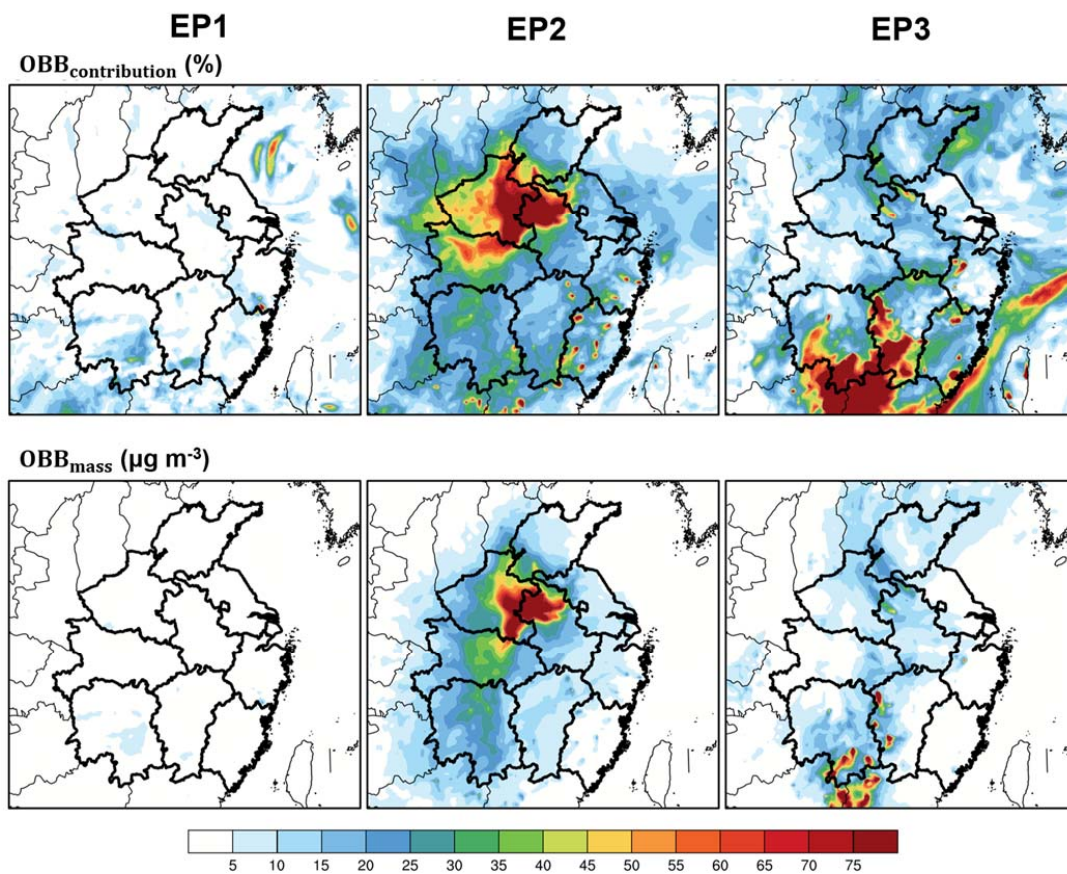


**Figure 8.** Spatial distributions of constrained  $PM_{2.5}$  emissions from (a) OCSB and (b) other types of OBB for the study period. This figure is generated using NCAR Command Language (NCL) version 6.3.0, open-source software free to the public.



40 Figure 9. Spatial distributions of  $OBB_{\text{mass}}$  and  $OBB_{\text{contribution}}$  during EP1, EP2 and EP3. This figure is generated using NCAR Command Language (NCL) version 6.3.0, open-source software free to the public.

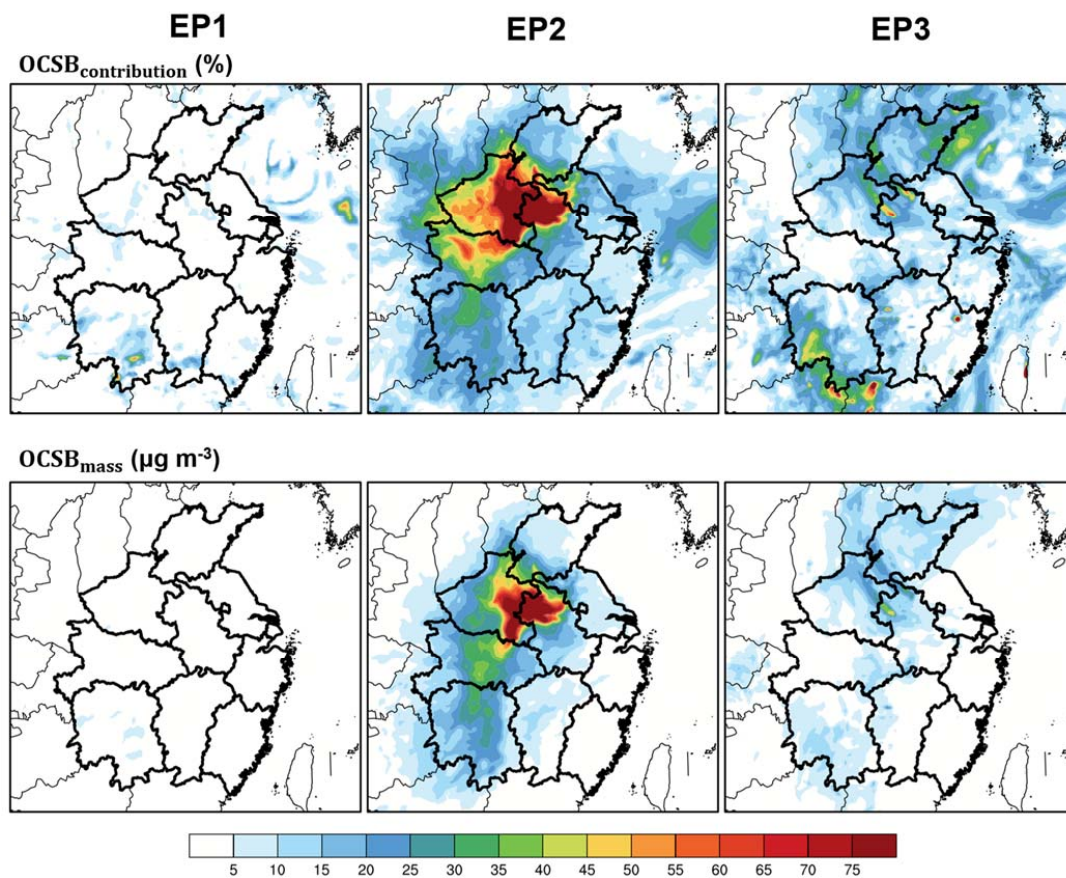


Figure 10. The same as Fig. 9 but for  $\text{OCSB}_{\text{mass}}$  and  $\text{OCSB}_{\text{contribution}}$ . This figure is generated using NCAR Command Language (NCL) version 6.3.0, open-source software free to the public.

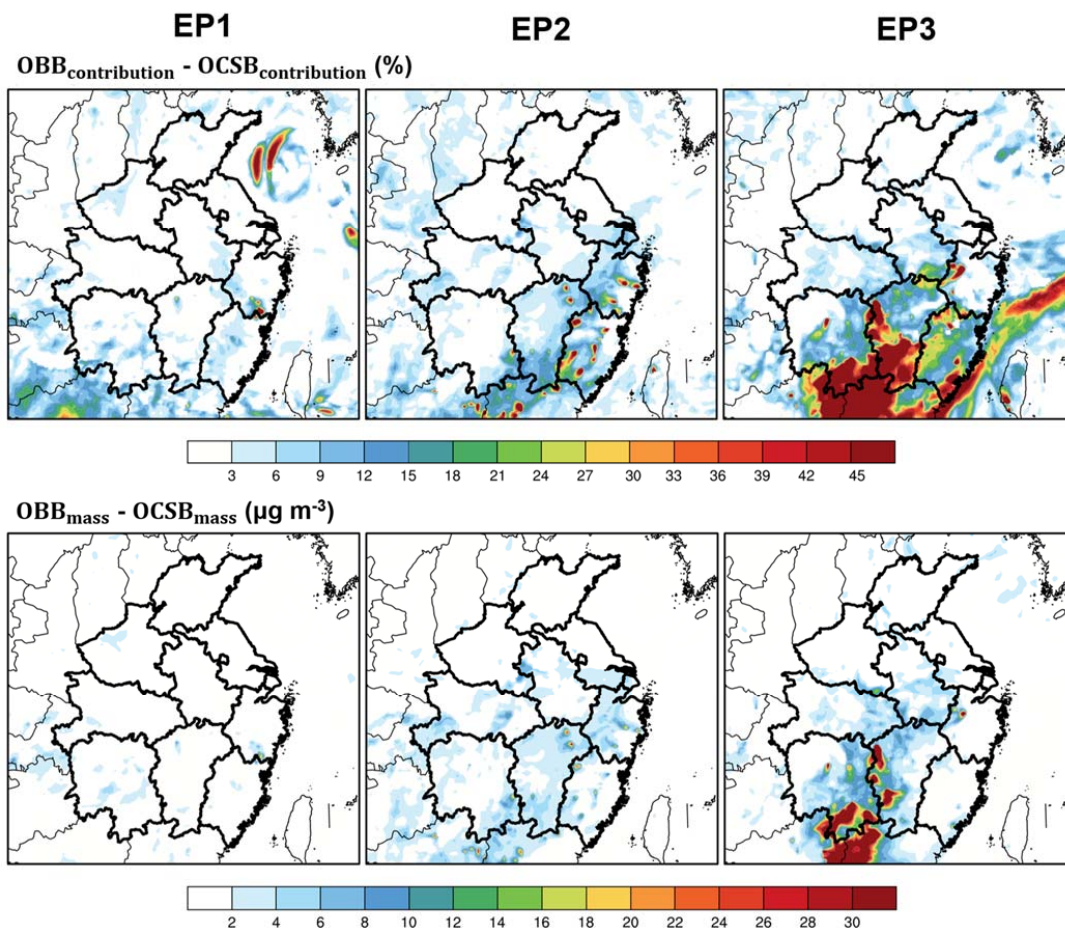


Figure 11. The same as Fig. 10 but for the differences between  $OBB_{mass}$  ( $OCSB_{mass}$ ) and  $OBB_{contribution}$  ( $OCSB_{contribution}$ ). This figure is generated using NCAR Command Language (NCL) version 6.3.0, open-source software free to the public.

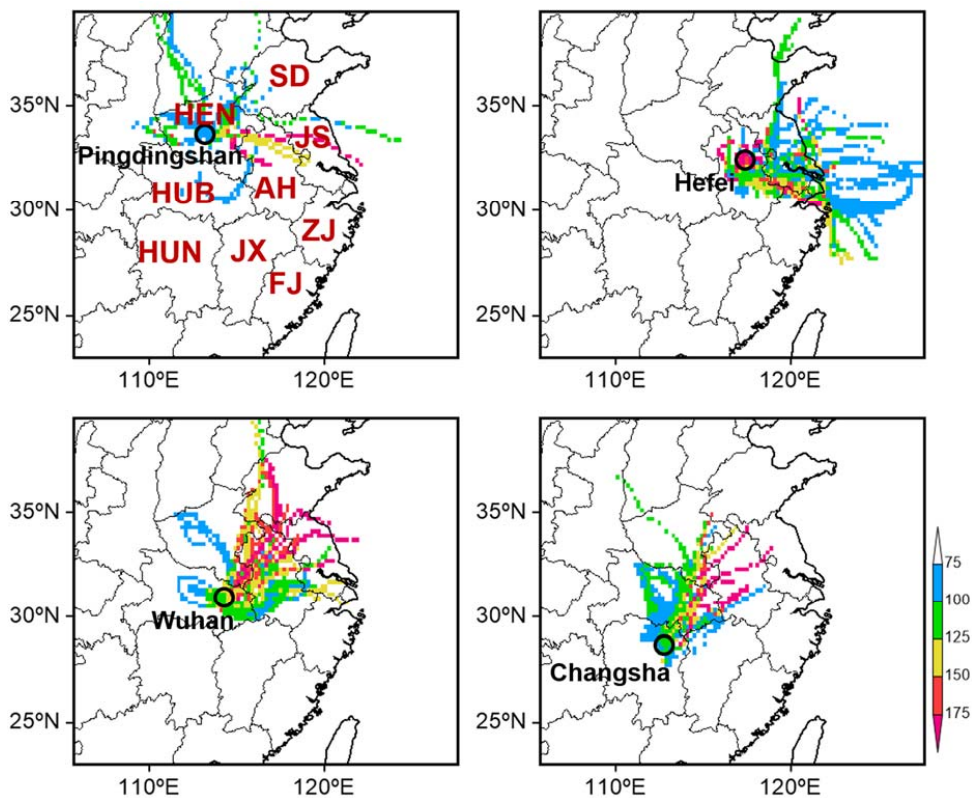


Figure 12. CWT maps during EP2 at four representative cities (Pingdingshan, Hefei, Wuhan and Changsha) that represent Henan, Anhui, Hubei and Hunan, respectively. This figure is generated using NCAR Command Language (NCL) version 6.3.0, open-source software free to the public.

55

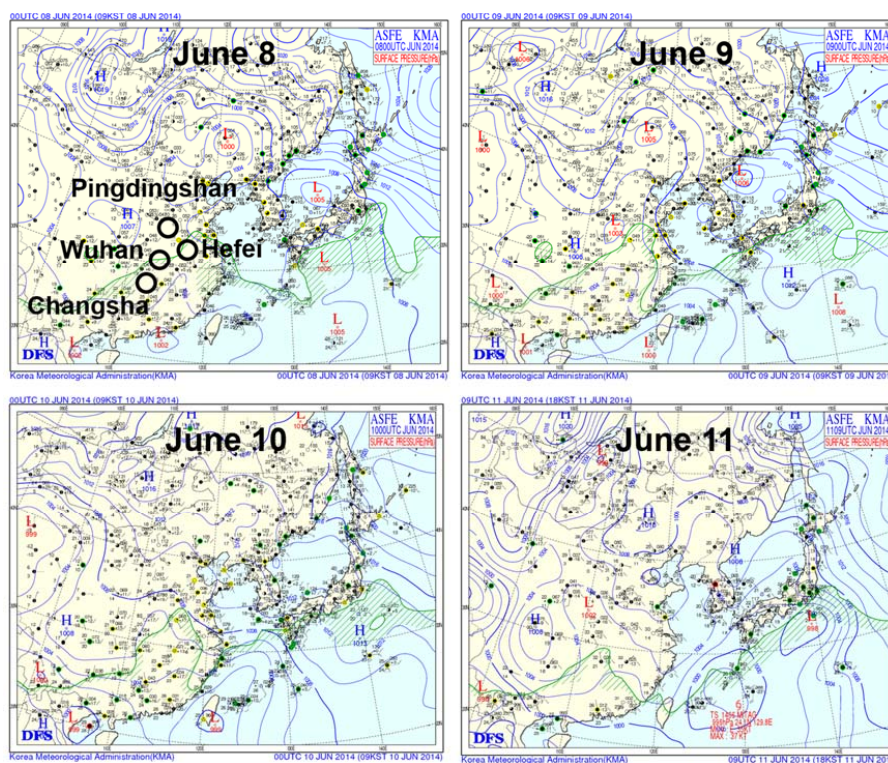
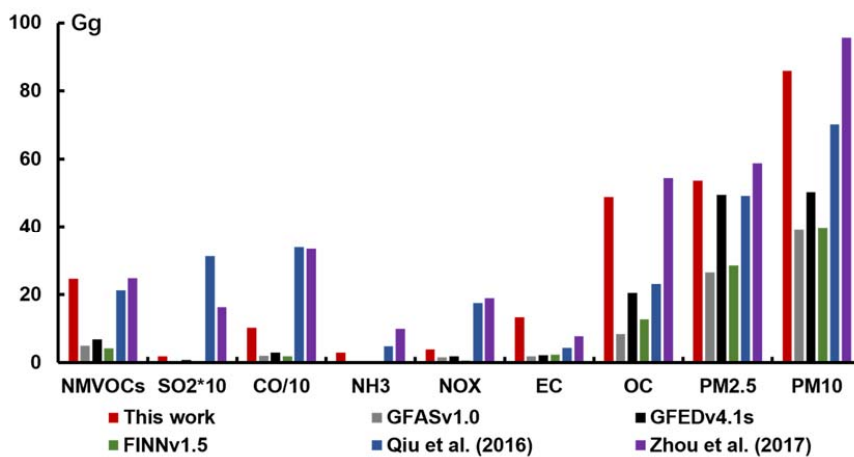


Figure 13. Surface weather maps for June 8, June 9, June 10, and June 11 over CEC (<http://www.kma.go.kr/eng/weather/images/analysischart.jsp>).



60

Figure 14. Comparisons of OBB emissions between other studies and this study.

65

70

75

80



Table 1. The constrained OBB and OCSB emissions for EP1, EP2, and EP3 for each province over CEC (Units: million moles for NMVOCs, SO<sub>2</sub>, CO, NH<sub>3</sub>, and NO<sub>x</sub> and tons for EC, OC, primary PM<sub>2.5</sub> and PM<sub>10</sub>).

Episode	Provinces	OBB										OCSB									
		NMVOCs	SO <sub>2</sub>	CO	NH <sub>3</sub>	NO <sub>x</sub>	EC	OC	PM <sub>2.5</sub>	PM <sub>10</sub>	NMVOCs	SO <sub>2</sub>	CO	NH <sub>3</sub>	NO <sub>x</sub>	EC	OC	PM <sub>2.5</sub>	PM <sub>10</sub>		
EP1	Shanghai	0	0	0	0	0	0	0	0	0	0	0	0	0	0	0	0	0	0	0	
	Jiangsu	16	0	58	2	2	10	49	88	107	16	0	56	2	2	10	46	82	99		
	Zhejiang	59	1	364	12	9	51	575	1107	1268	21	0	76	3	3	13	63	111	134		
	Anhui	66	0	245	8	9	43	219	387	473	64	0	226	8	8	39	188	331	401		
	Fujian	43	1	237	7	8	37	322	609	727	25	0	90	3	3	16	75	131	159		
	Jiangxi	34	1	197	6	6	31	291	527	622	20	0	72	2	3	13	60	106	128		
	Shandong	74	0	271	9	10	47	233	415	507	72	0	255	9	9	44	213	374	452		
	Henan	318	2	1155	39	43	201	978	1735	2111	315	2	1116	38	41	194	929	1633	1976		
	Hubei	40	0	158	5	6	28	155	266	326	39	0	137	5	5	24	114	201	243		
	Hunan	4	0	18	1	1	3	20	34	41	4	0	14	0	1	3	12	21	25		
EP2	Shanghai	60	1	262	8	10	47	284	492	609	55	0	194	7	7	34	162	284	344		
	Jiangsu	1104	7	4061	134	151	707	3549	6299	7681	1074	6	3809	130	141	663	3172	5575	6747		
	Zhejiang	397	7	2197	69	67	345	3129	5768	6785	242	1	857	29	32	149	714	1255	1519		
	Anhui	9485	54	33835	1147	1251	5890	28467	50126	60747	9430	53	33447	1140	1237	5824	27852	48953	59250		
	Fujian	241	5	1554	48	43	232	2496	4691	5556	83	0	295	10	11	51	246	432	523		
	Jiangxi	128	3	817	26	22	121	1301	2441	2835	50	0	179	6	7	31	149	262	317		
	Shandong	1311	8	4752	159	177	828	4019	7124	8667	1296	7	4597	157	170	800	3828	6729	8144		
	Henan	5000	29	17895	605	664	3116	15002	26467	32104	4975	28	17644	601	652	3072	14693	25824	31256		
	Hubei	64	1	271	9	9	45	299	538	645	54	0	193	7	7	34	161	282	342		
	Hunan	71	1	421	13	12	64	641	1197	1405	34	0	120	4	4	21	100	175	212		
EP3	Shanghai	0	0	0	0	0	0	0	0	0	0	0	0	0	0	0	0	0	0		
	Jiangsu	15	0	58	2	2	10	58	103	125	14	0	48	2	2	8	40	70	85		
	Zhejiang	24	0	129	4	4	19	186	355	411	12	0	43	1	2	7	36	63	76		
	Anhui	152	1	551	18	21	96	469	833	1012	149	1	530	18	20	92	441	775	939		
	Fujian	7	0	40	1	2	7	53	95	118	5	0	16	1	1	3	14	24	29		
	Jiangxi	59	1	393	13	10	57	643	1205	1394	21	0	73	2	3	13	61	107	129		
	Shandong	14	0	55	2	2	10	49	90	111	13	0	48	2	2	8	40	70	84		
	Henan	61	0	223	7	8	39	189	336	410	60	0	214	7	8	37	178	313	379		
	Hubei	7	0	28	1	1	5	29	52	65	6	0	22	1	1	4	18	32	39		
	Hunan	55	2	399	13	10	56	678	1299	1496	9	0	33	1	1	6	27	48	58		